Author(s)   Holopainen, Sami

Title   Influence of damage on inhomogeneous deformation behavior of amorphous glassy polymers. Modeling and algorithmic implementation in a finite element setting

Citation   Holopainen S. Influence of damage on inhomogeneous deformation behavior of amorphous glassy polymers. Modeling and algorithmic implementation in a finite element setting. Engineering fracture Mechanics (2014); 117C: pp. 28-50.

Year   2014

DOI   http://dx.doi.org/10.1016/j.engfracmech.2014.01.002

Version   Post-print

URN   http://URN.fi/URN:NBN:fi:tty-201406161308

Copyright

Influence of damage on inhomogeneous deformation behavior of amorphous glassy polymers. Modeling and algorithmic implementation in a finite element setting

Sami Holopainen

Tampere University of Technology, Department of Engineering Design

P.O.BOX 589, 33 101 Tampere, Finland, e-mail: `Sami.Holopainen@tut.fi`

Abstract

The objective of this work is to investigate the influence of damage mechanisms on inhomogeneous deformation behavior of amorphous glassy polymers. The mechanical properties of glassy polymers are strongly influenced by the microstructure which is typically described by network models. In order to improve the network model predictions at large multidimensional deformations, a distributed growth of void volume, crazing and possible disentanglement are investigated and considered in a part of the proposed viscoelastic-plastic model. The importance of different rheological properties employed in the model for regarding mechanical behavior is investigated and the role of damage in localized deformation is addressed. In order to evaluate the predictions of the proposed model, algorithmic constitutive equations are derived and implemented in a finite element program. The model is employed to the simulation of the cold drawing of dumbbell shaped test specimen.

1 Introduction

It is widely acknowledged that the macroscopic mechanical behavior of amorphous glassy polymers stems from three major microstructural characteristics: the number of entanglements and statistical links between the entanglements, the growth of shear bands and the extent of free volume around the chain molecules, cf. e.g. [1–4]. Moreover, amorphous glassy polymers exhibit several damage processes such as crazing, cavitation of impurities and micro-cracking within the matrix material. Onset of the volume changes in amorphous glassy polymers are the growth and coalescence of existing voids in addition to the nucleation and growth of new voids. Under compression, amorphous polymers frequently show ductile localized deformation, which is due to shear yielding with small volume changes. In contrast to the shear yielding mechanism, which involves shear band propagation and eventual fracture by a chain scission in large strains, the governing mechanism of inelastic deformation under tension is a dilatational localization in zones of fibrillation, termed crazing, cf. [5, 6].

[7] conducted plane strain compression tests both on polymethylmethacrylate (PMMA) and on polystyrene (PS) to investigate the formation of shear bands. According to their observations, the growth of shear bands is the primary source for the evolution of plastic deformation in amorphous glassy polymers. The plane strain tension tests by [8] showed a remarkable drop in the macroscopic stress immediately after the development of macroscopic shear bands. During continued deformation, the propagation of shear bands and the development of inhomogeneous deformation were observed which is macroscopically manifested by necking.

[9] investigated the influence of damage (crazing, cavitation of rubber particles and micro-cracking within the matrix material) on the plastic deformation and stability in polyethylene terephthalate (PET) and high-impact polystyrene (HIPS). Based on the optical micrographs, shear bands nucleated from the tips of existing crazes, rather than the crazes being nucleated

at the intersection of fine shear bands. They concluded that the onset of plastic deformation is initiation of crazing and the plastic stability is essentially controlled by damage processes such as craze-widening. To trigger a transition from crazing to shear yielding, some heterogeneity, which relieves the build-up of high hydrostatic stress, is needed in the amorphous structure, cf. [10]. In contrast to tensile tests, where the initial chain distribution have been found to be macroscopically uniform, large-scale molecular dynamics (MD) simulations have indicated that the chain distribution locally is heterogeneous, cf. [11]. As a result of heterogeneity, polymer material shows localized deformation where microscopic shear bands in closely packed regions develop and annihilate into macroscopic shear bands. [11] also showed that the thickness of the ligaments within the structure is crucial.

Despite all the active research carried out during the last decades, the governing micromechanism that controls crazing is still not fully understood. Experimental investigations have shown a major importance of the entanglement density in macroscopic failure through crazing or shear yielding, cf. e.g. [10, 12–14]. Initial plastic deformation through shear yielding in amorphous glassy polymers is usually followed by crazing or alternatively crazing propagates on stable manner, cf. [9, 15]. Examples of the polymers in the first group are e.g. polycarbonate (PC) and PMMA, and polymers involving stable crazing are e.g. HIPS and polyacrylonitrile-butadiene-styrene (ABS) that are frequently used in toughened polymer blends. According to [15], decrease of temperature and increase of the strain rate result in more brittle failure in amorphous glassy polymers, i.e. the difference between the time instants for craze-initiation and breakdown decreases. They also pointed out that the void nucleation is a precursor to crazing and crazes initiate due to high mean stress concentrations around the micro-voids. As a result of the damage processes, volume strains in relation to total strains, i.e. the plastic dilatation, was found to be significant. [16] conducted molecular dynamic MD simulations to investigate the role of deformation-induced disentanglement to void nucleation in amorphous glassy polymers. They concluded that disentanglement increases under highly triaxial stress states, which results in void nucleation being increased. They also pointed out that porous regions are created at the locations where almost all the polymer chains have slipped away except a few that are firmly anchored at their ends and pulled taut.

Most of the current models are based on the assumption that the plastic deformation only evolves because of the development and propagation of shear bands without volume changes. Concerning void growth, many of the inelastic damage models available for amorphous glassy polymers are based on the explicit knowledge of the yield surface involving a large number of material parameters to be identified, cf. [17–21]. However, the damage processes observed in amorphous glassy polymers are complex phenomena and their modeling seems to require such complexity. The models developed for metals have initially been considered for that purpose, cf. e.g. [22, 23]. Based on plane strain finite element simulations [24] investigated the effects of pressure sensitive yielding and plastic dilatancy on void growth and void mutual interaction. They concluded that void growth is promoted by pressure resulting higher porosity and void interaction in the material during loading. A widely used dilatational plasticity model is the one introduced by [25] and later modified by [26]. The Gurson model is based on the assumption that the deformation mode of the material surrounding a void is homogenous. According to this model, softening behavior in the material results from the growth of voids, i.e. the model does not possess the intrinsic ability to predict localized deformation by void coalescence.

The objective of this work is to investigate the influence of damage mechanisms on localized deformation of amorphous glassy polymers. Here, damage is ascribed to the distributed growth of void volume and crazing during plastic deformation. The concept of free volume is employed to describe the voids or the loosely packed regions in amorphous glassy polymers. In contrast

to rubber-toughened polymers, the void is considered as conceptual with no clear physical interpretation. However, since the voids are uniformly distributed in the material, the growth of voids is approximated by using the models which are conventionally applied to the modeling of void growth due to cavitation of small rubber particles or impurities present in polymer-rubber blends, cf. e.g. [19].

The specific model employed in this work is based on the celebrated 8-chain version of the [27] model, which is here termed the BPA model. In this Extended BPA (EBPA) model, both the elastic and plastic properties are considered as viscous. In order to evaluate the model predictions for inhomogeneous deformation, cold drawing experiments on PC were performed and the model was implemented in a finite element program. The EBPA model was calibrated to the force-displacement responses for inhomogeneous deformation acquired from cold drawing experiments on polycarbonate specimens. It was shown that the parameters which were obtained from calibration to homogeneous deformation cannot be used to satisfactorily predict the experimental response of inhomogeneous deformation. In order to find the mechanisms that are able to explain this discrepancy, the number of entanglements, possible disentanglement, void growth and crazing are investigated and considered in a part of the EBPA model. Macroscopic constitutive relations in the EBPA model are augmented by using a modified Gurson model, which also takes the nucleation of new voids into account. The role of damage mechanisms in strain localization is addressed and the importance of rheological properties employed in the model for regarding mechanical behavior is investigated.

2   Account of state-of-the-art network models

Many of state-of-the-art network models are shown to be in good agreement with experiments under monotonic loadings, cf. e.g. [28–32]. Moreover, most of the models include a moderate number of material parameters, which is of a great importance in practical applications.

2.1   Kinematics

Since state-of-the-art models mentioned above are based on the multiplicative split, the elements of this kinematical approach are briefly reviewed. According to the multiplicative split, the plastic deformation is defined through a local intermediate configuration and the deformation gradient $\boldsymbol{F}$ is decomposed into an elastic and a plastic component given by

$$\boldsymbol{F} = \boldsymbol{F}^{\mathrm{e}} \boldsymbol{F}^{\mathrm{p}} \tag{1}$$

where $\boldsymbol{F}^{\mathrm{p}}$ and $\boldsymbol{F}^{\mathrm{e}}$ define the elastic and plastic contribution, respectively, cf. [33]. Moreover, the deformation gradient can be given in terms of the rotation tensor $\boldsymbol{R}$ and the symmetric, positive definite stretch tensor $\boldsymbol{v}$ as

$$\boldsymbol{F} = \boldsymbol{v} \boldsymbol{R}. \tag{2}$$

The split in (1) provides the relation for the spatial velocity gradient $\boldsymbol{l}$, i.e.

$$\boldsymbol{l} := \dot{\boldsymbol{F}} \boldsymbol{F}^{-1} = \boldsymbol{l}^{\mathrm{e}} + \boldsymbol{l}^{\mathrm{p}} \tag{3}$$

where the elastic and plastic velocity gradients

$$\boldsymbol{l}^{\mathrm{e}} := \dot{\boldsymbol{F}}^{\mathrm{e}} \boldsymbol{F}^{\mathrm{e}-1}, \quad \boldsymbol{l}^{\mathrm{p}} := \boldsymbol{F}^{\mathrm{e}} \bar{\boldsymbol{L}}^{\mathrm{p}} \boldsymbol{F}^{\mathrm{e}-1}, \quad \bar{\boldsymbol{L}}^{\mathrm{p}} := \dot{\boldsymbol{F}}^{\mathrm{p}} \boldsymbol{F}^{\mathrm{p}-1} \tag{4}$$

3

were defined in the spatial and intermediate configuration, respectively. Specifically, the quantities in the intermediate configuration are highlighted by the bar. In the relations (3) and (4), a superposed dot denotes the material time derivative. In many applications, the decomposition of the spatial velocity gradient into it's symmetric and skew-symmetric parts is needed, i.e.

$$l = d + \omega \tag{5}$$

where the symmetric part $d := \mathrm{sym}(l)$ is the rate of deformation and $\omega := \mathrm{skew}(l)$ is the spin. Substitution of (3) in (5) allows the symmetric and skew-symmetric part of the elastic and plastic velocity gradients to be defined as

$$l^{\mathrm{e}} = d^{\mathrm{e}} + \omega^{\mathrm{e}}, \quad l^{\mathrm{p}} = d^{\mathrm{p}} + \omega^{\mathrm{p}}, \quad \bar{L}^{\mathrm{p}} = \bar{D}^{\mathrm{p}} + \bar{W}^{\mathrm{p}} \tag{6}$$

where

$$\begin{aligned} d^{\mathrm{e}} &:= \mathrm{sym}(l^{\mathrm{e}}), \quad \omega^{\mathrm{e}} := \mathrm{skew}(l^{\mathrm{e}}), \\ d^{\mathrm{p}} &:= \mathrm{sym}(l^{\mathrm{p}}), \quad \omega^{\mathrm{p}} := \mathrm{skew}(l^{\mathrm{p}}), \\ \bar{D}^{\mathrm{p}} &:= \mathrm{sym}(\bar{L}^{\mathrm{p}}), \quad \bar{W}^{\mathrm{p}} := \mathrm{skew}(\bar{L}^{\mathrm{p}}). \end{aligned} \tag{7}$$

For later use, the plastic deformation is given in terms of the plastic deformation tensor

$$\bar{C}^{\mathrm{p}} := F^{\mathrm{p}} F^{\mathrm{p,T}} \tag{8}$$

where the superscript, T, denotes the transpose. Based on (4) and (8) it is possible to extract the rate of the plastic deformation tensor $\dot{\bar{C}}^{\mathrm{p}}$, i.e.

$$\begin{aligned} \dot{\bar{C}}^{\mathrm{p}} &= \overline{\dot{F^{\mathrm{p}} F^{\mathrm{p,T}}}} = \dot{F}^{\mathrm{p}} F^{\mathrm{p,T}} + F^{\mathrm{p}} \dot{F}^{\mathrm{p,T}} = \dot{F}^{\mathrm{p}} F^{\mathrm{p-1}} F^{\mathrm{p}} F^{\mathrm{p,T}} + F^{\mathrm{p}} F^{\mathrm{p,T}} F^{\mathrm{p-T}} \dot{F}^{\mathrm{p,T}} \\ &= \bar{L}^{\mathrm{p}} \bar{C}^{\mathrm{p}} + \bar{C}^{\mathrm{p}} \bar{L}^{\mathrm{p,T}}. \end{aligned} \tag{9}$$

In many of state-of-the-art network models, the elastic constitutive description is given in terms of the elastic Finger tensor,

$$b^{\mathrm{e}} := F^{\mathrm{e}} F^{\mathrm{e,T}}, \tag{10}$$

defined in the spatial configuration. Taking advantage of (4), the rate of the elastic deformation tensor $\dot{b}^{\mathrm{e}}$ takes the following form

$$\begin{aligned} \dot{b}^{\mathrm{e}} &= \overline{\dot{F^{\mathrm{e}} F^{\mathrm{e,T}}}} = \dot{F}^{\mathrm{e}} F^{\mathrm{e,T}} + F^{\mathrm{e}} \dot{F}^{\mathrm{e,T}} = \dot{F}^{\mathrm{e}} F^{\mathrm{e-1}} F^{\mathrm{e}} F^{\mathrm{e,T}} + F^{\mathrm{e}} F^{\mathrm{e,T}} F^{\mathrm{e-T}} \dot{F}^{\mathrm{e,T}} \\ &= l^{\mathrm{e}} b^{\mathrm{e}} + b^{\mathrm{e}} l^{\mathrm{e,T}}. \end{aligned} \tag{11}$$

In accordance with (2), the polar decomposition of F^{e} allows to define the orientation of the intermediate configuration in terms of the left elastic stretch tensor

$$v^{\mathrm{e}} := \sqrt{b^{\mathrm{e}}} \tag{12}$$

and the elastic rotation R^{e}, i.e.

$$F^{\mathrm{e}} = v^{\mathrm{e}} R^{\mathrm{e}}. \tag{13}$$

Similar to (13), use is made of the polar decomposition of the plastic deformation gradient,

$$F^{\mathrm{p}} = \bar{V}^{\mathrm{p}} R^{\mathrm{p}}, \tag{14}$$

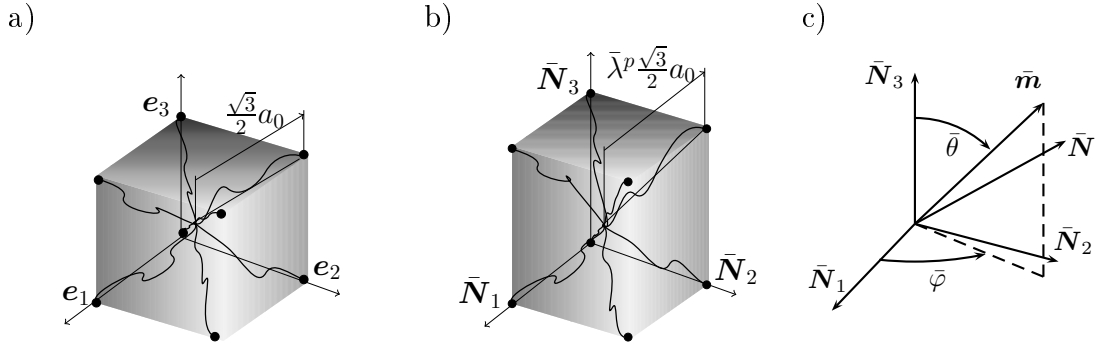where R^{p} is the plastic rotation and $\bar{V}^{\mathrm{p}}$ is the plastic stretch defined in the intermediate configuration.

Figure 1: The chain geometry according to the 8-chain model in a) undeformed and b) deformed configuration. The base vectors $\bar{\boldsymbol{N}}_\alpha$, $\alpha = 1, 2, 3$, align with the unit eigenvectors of $\bar{\boldsymbol{V}}^p$. The dimension of the undeformed element is a_0 and $\bar{\lambda}^p$ denotes the plastic chain stretch which appears in the direction $\bar{\boldsymbol{m}}$. The unit vector $\bar{\boldsymbol{m}}$ is defined by the angles $\bar{\theta}$ and $\bar{\varphi}$, whereas the plastic network stretch λ^p_{ec} is related to the direction $\bar{\boldsymbol{N}} := 1/\sqrt{3} \sum_\alpha \bar{\boldsymbol{N}}_\alpha$.

2.2 Specific constitutive model

Even if state-of-the-art network models are shown to be predictive under monotonic loadings, a comparison with the experimental data reveals that they fail to capture a nonlinear response during repeated or cyclic loadings, cf. [31, 32]. Moreover, under long-term loadings, the models typically predict an overestimated recovery and creep. In order to improve the model predictions under these conditions, we have proposed an extension of the BPA model termed the EBPA model, cf. [34]. In contrast to referred state-of-the-art models, the EBPA model includes both viscoelastic and viscoplastic ingredients needed to compensate for the shortcomings of state-of-the-art models.

As with the BPA model, the microstructure in the EBPA model is represented by an overall chain network which consists of cubic cells, cf. Fig. 1. The segments of eight molecular chains extend from the center point of the cubic cell along its diagonals. In large deformations, the chains align with the principal plastic stretches of continuum and results in an highly anisotropic response, cf. [28].

Fig. 2 shows a rheological presentation of the EBPA model which consists of an elastic spring a) in series with two Kelvin-Voigt elements. The upper Kelvin-Voigt element involves an elastic spring b) and a viscous dashpot c), both being solely affected by the elastic deformations. The Kelvin-Voigt element is employed for predicting creep and recovery, while its combination with the elastic spring a) is aimed at describing the stress relaxation. The second Kelvin-Voigt-like element comprises two viscoplastic dashpots d) arranged parallel with a nonlinear spring e) which results in the evolution of anisotropy in large strains.

To improve the accuracy of the linear viscoelastic models in large multi-dimensional deformations, the multiplicative split of the elastic deformation
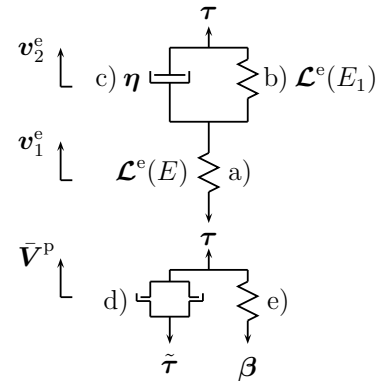

Figure 2: Rheological representation of the EBPA model involving the elements: two elastic springs a) and b), a viscoelastic dashpot c), two viscoplastic dashpots d) and a nonlinear Langevin spring e). Difference between the Kirchhoff stress $\boldsymbol{\tau}$ and the backstress $\boldsymbol{\beta}$ defines the driving stress $\tilde{\boldsymbol{\tau}}$.

gradient $\boldsymbol{F}^{\mathrm{e}}$ into a viscous and an elastic part is applied, i.e.

$$\boldsymbol{F}^{\mathrm{e}} = \boldsymbol{F}^{\mathrm{e}}_1 \boldsymbol{F}^{\mathrm{e}}_2 \tag{15}$$

where $\boldsymbol{F}^{\mathrm{e}}_1$ and $\boldsymbol{F}^{\mathrm{e}}_2$ define the elastic stretching in the spring a) and b), respectively, cf. Fig. 2. The polar decomposition of $\boldsymbol{F}^{\mathrm{e}}_1$ and $\boldsymbol{F}^{\mathrm{e}}_2$ allows to define the orientation of the intermediate elastic configuration as

$$\boldsymbol{F}^{\mathrm{e}}_1 = \boldsymbol{v}^{\mathrm{e}}_1 \boldsymbol{R}^{\mathrm{e}}_1 \quad \text{and} \quad \boldsymbol{F}^{\mathrm{e}}_2 = \boldsymbol{v}^{\mathrm{e}}_2 \boldsymbol{R}^{\mathrm{e}}_2 \tag{16}$$

where $\boldsymbol{R}^{\mathrm{e}}_1$ and $\boldsymbol{R}^{\mathrm{e}}_2$ are the elastic rotations and $\boldsymbol{v}^{\mathrm{e}}_1$ and $\boldsymbol{v}^{\mathrm{e}}_2$ are the elastic stretch tensors, defined in the spatial and the elastic intermediate configuration, respectively. The split of the elastic deformation gradient (16) is depicted in Fig. 3.

Taking notice of the stress equilibrium as shown in Fig. 2, the elastic constitutive law is given as

$$\boldsymbol{\tau} = \boldsymbol{\mathcal{L}}^{\mathrm{e}}(E) : \ln \boldsymbol{v}^{\mathrm{e}}_1 = \boldsymbol{\eta} : \frac{d}{dt}(\ln \boldsymbol{v}^{\mathrm{e}}_2) + \boldsymbol{\mathcal{L}}^{\mathrm{e}}(E_1) : \ln \boldsymbol{v}^{\mathrm{e}}_2 \tag{17}$$

where the Young's moduli E and E_1 relate to the elastic springs a) and b), respectively. Using the shear modulus $\mu := E/2(1 + \nu)$ and the bulk modulus $\kappa := E/3(1 - 2\nu)$, the fourth order elasticity tensor is defined as

$$\boldsymbol{\mathcal{L}}^{\mathrm{e}} := 2\mu(\boldsymbol{\mathcal{I}} + \frac{3\kappa - 2\mu}{6\mu}\boldsymbol{i} \otimes \boldsymbol{i}) \tag{18}$$

where ν is the Poisson's ratio and $\boldsymbol{i}$ and $\boldsymbol{\mathcal{I}}$ are the spatial second and fourth order identity tensors, respectively. The components of $\boldsymbol{\mathcal{L}}^{\mathrm{e}}$ in an orthonormal cartesian coordinate system take the form

$$\mathcal{L}^{\mathrm{e}}_{\mathrm{ijkl}} := 2\mu \left[\frac{1}{2} \left(\delta_{\mathrm{ik}}\delta_{\mathrm{jl}} + \delta_{\mathrm{il}}\delta_{\mathrm{jk}} \right) + \frac{3\kappa - 2\mu}{6\mu}\delta_{\mathrm{ij}}\delta_{\mathrm{kl}} \right] . \tag{19}$$

In general, the stiffness of the viscous damper $\boldsymbol{\eta}$ is regarded as a fourth order tensor, given as

$$\boldsymbol{\eta} = \eta_1 \boldsymbol{\mathcal{I}} + \eta_2 \boldsymbol{i} \otimes \boldsymbol{i}$$

where η_1 and η_2 are viscosities that govern elastic shear and volumetric deformation, respectively. They may also depend on temperature and the elastic strain rate, cf. [35]. Assuming η to be a scalar, only three new material parameters h_2, E_1 and η enter the proposed model.

Since the proposed model relies on the assumption of small elastic stretches in relation to the plastic stretches, the rate of plastic deformation $\bar{\boldsymbol{D}}^{\mathrm{P}}$ is taken to align with the spatial normalized direction of $\tilde{\boldsymbol{\tau}}^{\mathrm{dev}}$, i.e.

$$\bar{\boldsymbol{D}}^{\mathrm{p}} := \frac{\dot{\gamma}^{\mathrm{p}}}{\sqrt{2}}\boldsymbol{n}, \quad \boldsymbol{n} = \frac{\tilde{\boldsymbol{\tau}}^{\mathrm{dev}}}{\tau}, \quad \tilde{\boldsymbol{\tau}}^{\mathrm{dev}} := \boldsymbol{\tau}^{\mathrm{dev}} - \boldsymbol{\beta}^{\mathrm{dev}}, \quad \tau := \sqrt{\frac{1}{2}\tilde{\boldsymbol{\tau}}^{\mathrm{dev}} : \tilde{\boldsymbol{\tau}}^{\mathrm{dev}}} \tag{20}$$

where $\boldsymbol{\beta}$ is the backstress and $\dot{\gamma}^{\mathrm{p}}$ is defined subsequently. The superscript, dev, denotes the deviatoric component. In contrast to the BPA model, in which the flow rule is postulated in terms of the Cauchy stress $\boldsymbol{\sigma}$, the Kirchhoff stress $\boldsymbol{\tau} = J^{\mathrm{e}}\boldsymbol{\sigma}$ is applied in the EBPA model. This choice is motivated by the shear-type flow rule (20) where the volumetric deformation is suppressed. Noting that $\bar{\boldsymbol{D}}^{\mathrm{P}}$ turns out to be deviatoric, the trace of (6)$_3$ yields

$$\text{trace}(\bar{\boldsymbol{L}}^{\mathrm{P}}) = \text{trace}(\bar{\boldsymbol{D}}^{\mathrm{P}}) + \text{trace}(\bar{\boldsymbol{W}}^{\mathrm{P}}) = 0, \tag{21}$$

which reveals that the plastic deformation is isochoric, i.e. $J^{\mathrm{p}} := \det(\boldsymbol{F}^{\mathrm{p}}) = 1$. It then follows that $J = J^{\mathrm{e}} := \det(\boldsymbol{F}^{\mathrm{e}})$. In terms of a non-affine plastic network stretch

$$\lambda^{\mathrm{p}}_{\mathrm{ec}} := \sqrt{\text{trace}(\bar{\boldsymbol{C}}^{\mathrm{P}})/3} \tag{22}$$
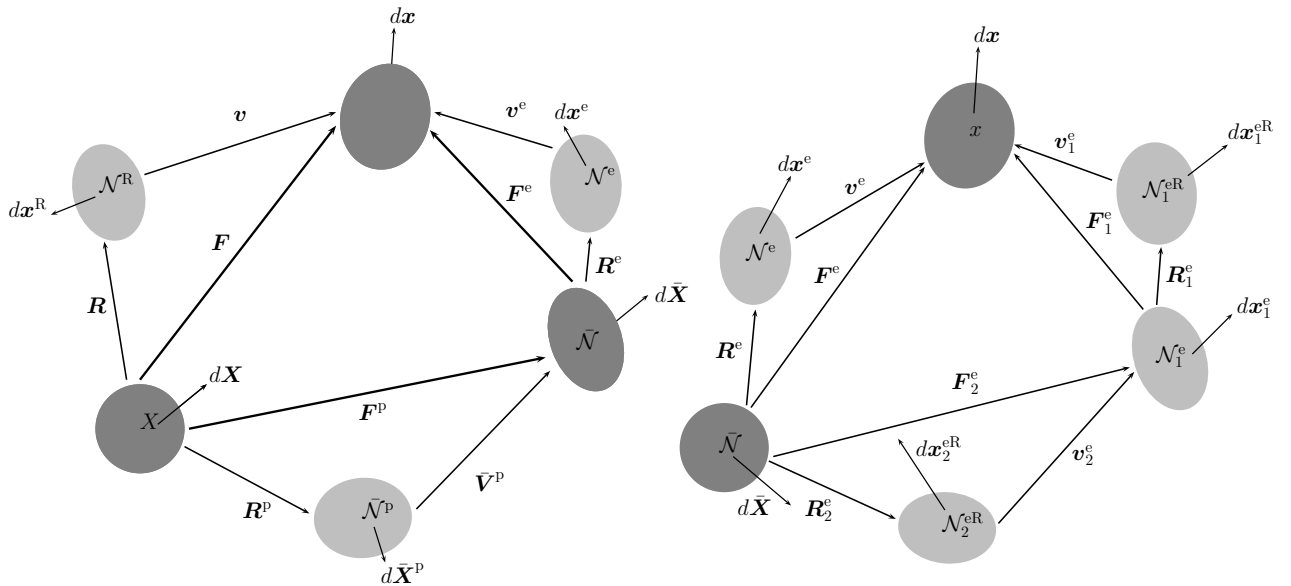
6

Figure 3: Deformation of a solid body and the mappings between different configurations. The polar decomposition of the deformation gradient based on the left stretches $\boldsymbol{v}$, $\bar{\boldsymbol{V}}^p$ and $\boldsymbol{v}^e$ (left). The split of the elastic deformation gradient $\boldsymbol{F}^e$ into the elastic and viscous part $\boldsymbol{F}_1^e$ and $\boldsymbol{F}_2^e$ (right). In terms of the left stretches $\boldsymbol{v}^e$, $\boldsymbol{v}_1^e$ and $\boldsymbol{v}_2^e$, the polar decompositions are also presented.

and the inverse Langevin function $\chi := \mathfrak{L}^{-1}(\lambda_{\text{ec}}^{\text{p}}/\sqrt{N})$, the anisotropic hardening in the EBPA model is described by the backstress. In the intermediate configuration, the principal components are given by

$$\bar{B}_\alpha^{\text{dev}} = \frac{C_{\text{R}}}{3\lambda_{\text{ec}}^{\text{p}}}\sqrt{N}\mathfrak{L}^{-1}(\frac{\lambda_{\text{ec}}^{\text{p}}}{\sqrt{N}})\big((\bar{\lambda}_\alpha^{\text{p}})^2 - (\lambda_{\text{ec}}^{\text{p}})^2\big), \quad \alpha = 1, 2, 3, \tag{23}$$

where C_{R} is a material parameter, $\bar{\lambda}_\alpha^{\text{p}}$ are the principal plastic stretches and N is the number of statistical links of length l between the physical entanglements. According to non-Gaussian chain statistics, the finite extensibility of chain is $r_{\text{L}} = Nl$ while the undeformed length is $r_0 = \sqrt{N}l$ and thus the chain locking stretch is given by $\lambda_{\text{L}} = r_{\text{L}}/r_0 = \sqrt{N}$. The spatial form of the deviatoric backstress $\boldsymbol{\beta}^{\text{dev}}$ needed in (20) is obtained by push-forwarding $\bar{\boldsymbol{B}}^{\text{dev}}$ by $\boldsymbol{F}^e$. The inverse Langevin function present in (23) results in a strong increase in the backstress as the stretch in the chains reaches the limit λ_{L}.

The mechanical behavior of amorphous glassy polymers is described by an almost elastic initial response which is followed by strain softening and subsequent strain hardening. This "S-shaped" behavior in the EBPA model results from mixed isotropic and kinematic hardening. The isotropic hardening is due to the intermolecular resistance to chain segment rotation and it is modeled by two viscoplastic dashpots, cf. element d) in Fig. 2. The evolution of the plastic deformation is governed by

$$\dot{\gamma}^{\text{p}} = \dot{\gamma}_0 \exp\big(-\frac{As_{\text{s}}}{T}(1 - (\frac{\tau}{J^e s_{\text{s}}})^{\frac{5}{6}})\big), \tag{24}$$

cf. [1]. Later, [27] extended a constant athermal shear stress s_{s} to include the pressure effect by taking $s_{\text{s}} = s + \alpha p$ to evolve to the saturation value s_{ss}. In equation (24), $\dot{\gamma}_0$ is a pre-exponential factor, A is proportional to the activation volume, $p = -\text{trace}(\boldsymbol{\sigma})/3$ is the pressure, α is a pressure dependence factor and T is the absolute temperature. The extra dashpot is aimed at increasing the isotropic hardening effect and thereby suppress the influence of kinematic hardening. The original and extra dashpot are modeled by the two internal state variables s_1 and s_2 giving an additional increase to the shear resistance, i.e.

$$s = s_1 + s_2. \tag{25}$$

7

Table 1: Summary of the EBPA model.

---

1. Kinematics: $\boldsymbol{F} = \boldsymbol{F}^{\mathrm{e}}\boldsymbol{F}^{\mathrm{p}}, \quad \boldsymbol{F}^{\mathrm{e}} = \boldsymbol{F}_1^{\mathrm{e}}\boldsymbol{F}_2^{\mathrm{e}} = \boldsymbol{v}^{\mathrm{e}}\boldsymbol{R}^{\mathrm{e}}, \quad \boldsymbol{R}^{\mathrm{e}}$ is unity, $\quad \boldsymbol{b}_1^{\mathrm{e}} := \boldsymbol{F}_1^{\mathrm{e}}\boldsymbol{F}_1^{\mathrm{e,T}},$

$\qquad \boldsymbol{v}_1^{\mathrm{e}} := \sqrt{\boldsymbol{b}_1^{\mathrm{e}}}, \quad \boldsymbol{R}_1^{\mathrm{e}}$ is unity, $\quad \boldsymbol{b}_2^{\mathrm{e}} := \boldsymbol{F}_2^{\mathrm{e}}\boldsymbol{F}_2^{\mathrm{e,T}}, \quad \boldsymbol{v}_2^{\mathrm{e}} := \sqrt{\boldsymbol{b}_2^{\mathrm{e}}}, \quad \bar{\boldsymbol{C}}^{\mathrm{p}} := \boldsymbol{F}^{\mathrm{p}}\boldsymbol{F}^{\mathrm{p,T}}.$

2. Stress: $\quad \boldsymbol{\tau} := 2\mu(\ln \boldsymbol{v}_1^{\mathrm{e}})^{\mathrm{dev}} + \kappa \ln J_1^{\mathrm{e}}\boldsymbol{i}, \;\; J_1^{\mathrm{e}} = \det(\boldsymbol{F}_1^{\mathrm{e}}).$

3. Micro-macro transition: $\quad \lambda_{\mathrm{ec}}^{\mathrm{p}} = \dfrac{1}{\sqrt{3}}\sqrt{\mathrm{trace}(\bar{\boldsymbol{C}}^{\mathrm{p}})} \in (0, \sqrt{N}).$

4. Flow rule: $\quad \bar{\boldsymbol{D}}^{\mathrm{p}} = \dot{\gamma}^{\mathrm{p}}\boldsymbol{n}, \quad \boldsymbol{n} := \dfrac{\tilde{\boldsymbol{\tau}}^{\mathrm{dev}}}{\sqrt{2}\tau}, \quad \tilde{\boldsymbol{\tau}}^{\mathrm{dev}} := \boldsymbol{\tau}^{\mathrm{dev}} - \boldsymbol{\beta}^{\mathrm{dev}}, \quad \tau := \sqrt{\dfrac{1}{2}\tilde{\boldsymbol{\tau}}^{\mathrm{dev}} : \tilde{\boldsymbol{\tau}}^{\mathrm{dev}}}.$

5. Backstress: $\quad \bar{\boldsymbol{B}}^{\mathrm{dev}} = \dfrac{C^{\mathrm{R}}}{3\lambda_{\mathrm{ec}}^{\mathrm{p}}}\sqrt{N}\mathcal{L}^{-1}(\dfrac{\lambda_{\mathrm{ec}}^{\mathrm{p}}}{\sqrt{N}})(\bar{\boldsymbol{C}}^{\mathrm{p}})^{\mathrm{dev}}$ push-forward $\rightarrow \; \boldsymbol{\beta}^{\mathrm{dev}}$

6. Isotropic hardening: $\quad \dot{\gamma}^{\mathrm{p}} := \dot{\gamma}_0 \exp\!\big(-\dfrac{As_s}{T}(1 - (\dfrac{\tau}{J^{\mathrm{e}}s_s})^{\frac{5}{6}})\big), \;\; J^{\mathrm{e}} = \det(\boldsymbol{F}^{\mathrm{e}}), \;\; p = -\dfrac{1}{3}\mathrm{trace}(\boldsymbol{\sigma}),$

$\qquad s_s = s + \alpha p, \;\; s$ is given by (25) and (26), and $s(0) = s_0.$

The internal variables s_1 and s_2 evolve according to

$$
\begin{aligned}
\dot{s}_1 &= h_1(1 - s_1/s_{\mathrm{ss}})\dot{\gamma}^{\mathrm{p}}, \quad s_1(0) = s_0, \\
\dot{s}_2 &= h_2(1 - \mathcal{H}(s_2 - \bar{s}_2))\dot{\gamma}^{\mathrm{p}}, \quad s_2(0) = 0
\end{aligned}
\tag{26}
$$

where the parameters h_1 and h_2 control the approach of s_1 and s_2 to s_{ss} and $\bar{s}_2$, respectively. $\mathcal{H}$ is the Heaviside-function which prevents an excessive hardening e.g. during cyclic loading. The threshold argument $\bar{s}_2$ can be found experimentally.

Taking note of (24) and $(26)_2$ reveals that $\dot{s}_2$ is positive and thus, s_2 is monotonically increasing. It then follows that the amount of isotropic hardening in relation to the amount of kinematic hardening increases and as a result the evolution of the backstress suppresses in the EBPA model. A reduced evolution of the backstress is of major importance at a low-stress level, where the plastic evolution is particularly governed by the backstress. The EBPA model is summarized in Table 1.

2.3 Calibration of the EBPA model to homogeneous deformation

In order to evaluate the capability of the EBPA model, uniaxial compression tests involving complex loading situations were simulated. The parameters employed in the simulations are listed in Table 2. Fig. 4 shows capability of both the original BPA model and the EBPA model to predict the true stress vs strain response under repeated unloadings. Even if the EBPA model overpredicts recovery during the first cycle, it is superior to the BPA model during subsequent cycles. Since the EBPA model has been shown to well capture the experimental response during complex loading situations, cf. also [34], the subsequent considerations will be based on this model.
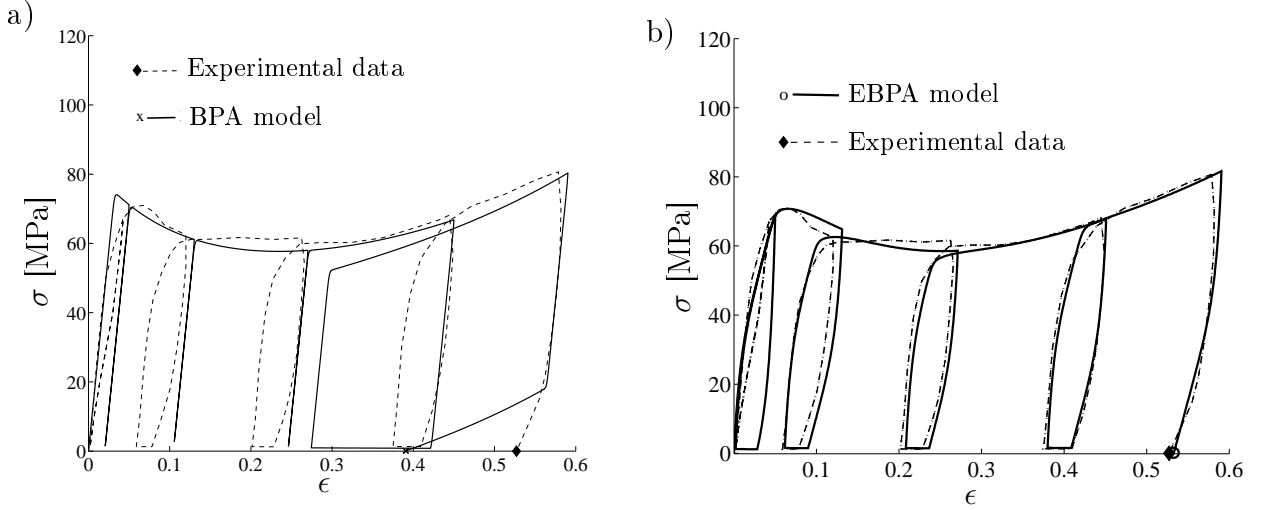
Figure 4: Uniaxial compression response for bisphenol A polycarbonate according to a) the BPA model and b) the EBPA model. The repeated unloadings are performed to progressively increasing strain levels $\epsilon = 0.05$, 0.13, 0.27, 0.45 and 0.59 and then the stress level $\sigma = 1.2$ MPa is kept fixed for a dwell time 12,000 s. Experimental data is taken from [31].

3 Investigation of necking of dumbbell shaped specimen

To evaluate the capability of the EBPA model and its numerical implementation to predict inhomogeneous deformation behavior, cold drawing experiments on PC-specimen were conducted. Cold drawing, which typically results in neck propagation on a amorphous glassy polymers, is frequently used method for the production of anisotropy in polymers. The tests were performed by using the Instron© 5967 tension/compression electromechanical testing machine controlled by Blue Hill 3 software. A layout of the testing arrangement is shown in Fig. 5.

The test specimen under consideration is dumbbell-shaped and it is fabricated from Lexan® 223R PC-polymer. During drawing, the applied load f and the elongation u were monitored. To prevent an increase in temperature due to the dissipative heating, a slow cross head speed $\dot{u} = 2$ mm/min was applied. Moreover, the elongation of the specimen was restricted to $u = 0.3L \approx 40$ mm to avoid localized deformation at the interface of the gauge section and the grips. A more detailed account for the test program involving repeated loading cycles is found from [34].

Snapshots of the dumbbell shaped test specimen during drawing are depicted in Fig. 6. The selected stages of deformation show the initiation, stabilization and propagation of neck. The

Table 2: Constitutive parameters of the BPA and EBPA model for bisphenol A polycarbonate (BPA-PC) and PC. Moreover, $E_1 = 0.3E$ in the EBPA model. The parameters for BPA-PC are obtained from the calibration to uniaxial compression tests performed at room temperature under monotonic loading, cf. [31]. The calibration of the EBPA model on PC is based on the uniaxial and plane strain compression experiments given in [28]. The BPA model parameters for PC are taken from [36].

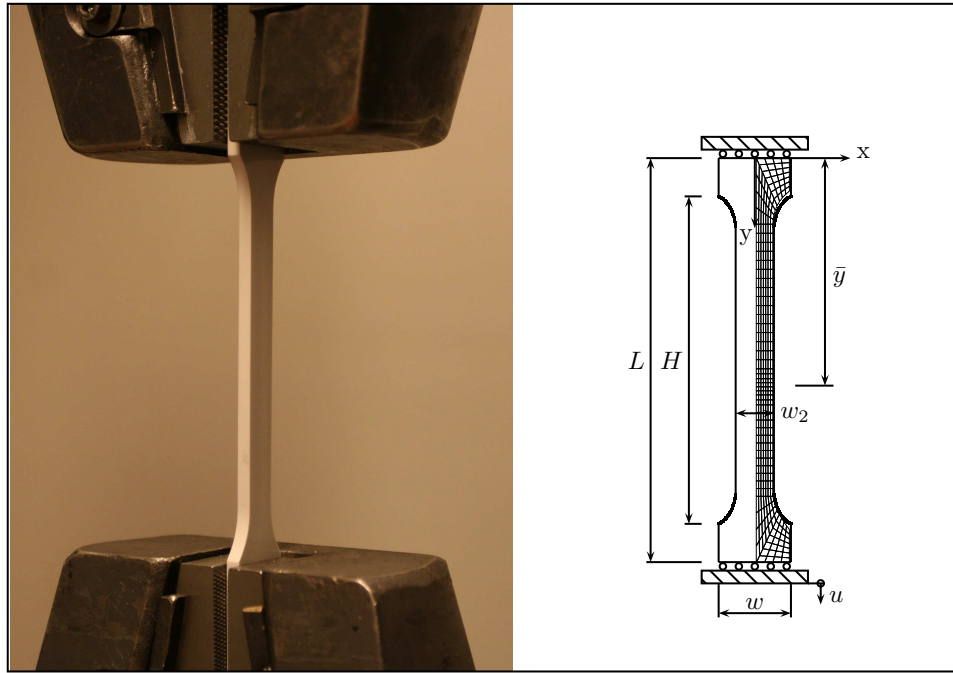|	E	η	s_0	s_{ss}	h_1	h_2	$\dot{\gamma}_0$	A	C^{R}	N	α
BPA-PC	MPa	MPas	MPa	MPa	MPa	MPa	s^{-1}	MPa^{-1}K	MPa		
BPA	2300		99	73.0	370		$2 \cdot 10^{15}$	241	14.0	1.85	0.08
EBPA	3700	$5.0 \cdot 10^4$	100	56.5	205	40	$5.6 \cdot 10^{15}$	241	14.0	2.20	0.08
PC	MPa	MPa	MPa	MPa	MPa	s^{-1}	MPa^{-1}K	MPa			
BPA	2300		97	76.6	500		$2.0 \cdot 10^{15}$	240	12.8	2.15	0.08
EBPA	3300	$6.0 \cdot 10^4$	96	61.0	170	10	$5.4 \cdot 10^{15}$	240	17.8	2.42	0.08

Figure 5: The illustration of the testing arrangement. The displacement at $y = 0$ is fixed by a grip and the elongation u at the other end $y = L$ is prescribed. The geometry of the dumbbell-shaped test specimen is given by $H/L \approx 0.90$, $w/L \approx 0.17$, $w_2/L \approx 0.09$ and $t/L \approx 0.035$ where t is the specimen's thickness. The details of the specimen's geometry are specified in ISO 527-2. The shown finite element discretization is of a mesh with 4-node plane elements.

neck in the test specimen is rather diffuse, i.e. the localized zone extends and reaches rapidly the end of the gauge section.

The EBPA model was calibrated to the force-displacement responses acquired from the cold drawing experiments on polycarbonate specimens. To trigger the localization in the simulation of the test, a small initial imperfection was introduced

$$\Delta w_2 = w_2 \xi_0, \tag{27}$$

i.e. the width of the gauge section at $y = \bar{y}$ is $w_2 - \Delta w_2$, cf. Fig. 5. During the experiment, neck was observed to initiate near the center of the specimen, i.e. $\bar{y} = L/2$. In calibration, the plane strain mode, especially in the gauge section, was assumed to be accurate enough.

Due to the symmetry of the geometry and boundary conditions, only a quarter of the specimen was considered in the numerical analysis. The finite element discretization employed is of a mesh

Table 3: The values of the EBPA and the BPA model parameters. Moreover, $E_1 = 0.3E$ in the EBPA model. Calibration of the models is based on the cold drawing experiments of the dumbbell-shaped PC-specimen. The intensity of the initial imperfection in (27) is set to $\xi_0 = 0.002$.

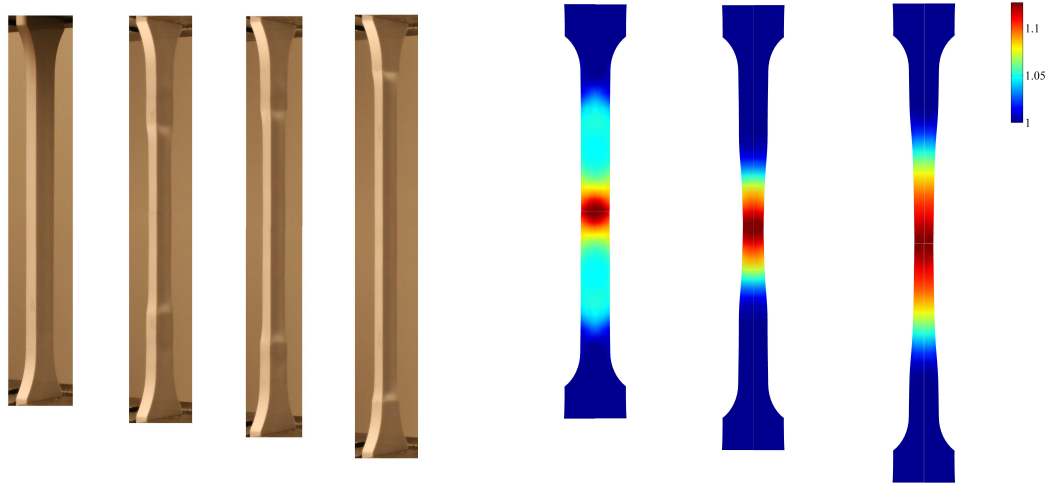|	E	η	s_0	s_{ss}	h_1	h_2	$\dot{\gamma}_0$	A	C^{R}	N	α
	MPa	MPas	MPa	MPa	MPa	MPa	s^{-1}	$MPa^{-1}K$	MPa		
EBPA	2550	$1.5 \cdot 10^5$	96	76	720	40	$5.6 \cdot 10^{15}$	241	14	2.2	0.08
BPA	2300		99	73	370		$2 \cdot 10^{15}$	241	14.0	1.85	0.08

10

Figure 6: Snapshots of a dumbbell shaped test specimen during elongation: $u = 10$ mm, $u = 20$ mm, $u = 30$ mm and at the end of the loading $u = 40$ mm. Based on the EBPA model the deformed shapes are visualized by the plastic stretch $\bar{\lambda}_{ec}^{p}$ at three different phases: $u = 10$ mm, $u = 20$ mm and at the end of the loading. The finite element discretization employed is of a mesh with 4-node plane elements.

with 196 4-node plane elements. The numerical treatment of the model is discussed in Appendix A. The calibrated parameters are given in Table 3. For later purposes, also the BPA model parameters, which were obtained from the calibration to the same data, are presented in Table 3.

The numerical investigations indicated that the original BPA model is relative-well able to predict the inhomogeneous deformation behavior by using the material parameters obtained from the calibration to a homogeneous deformation mode. As far as the EBPA model is concerned, comparison of Tables 2 and 3 reveals that the parameters which were obtained from calibration for homogeneous deformation cannot be used to satisfactorily predict the experimental response of inhomogeneous deformation. Even if the material of the specimen slightly differing from the PC-polymer employed in the tests for homogeneous deformation, this discrepancy cannot entirely be explained either by the localization phenomena or boundary effects.

To investigate the influence of neglected volume changes (geometric softening) on the neck propagation, the EBPA model was also implemented in a three-dimensional finite-element code. The finite element discretization consists of a mesh with 8-node linear hybrid brick elements with constant pressure. Based on the two and three dimensional finite element analyses, Figs. 6 and 7 show the deformed shapes of the specimen during drawing. As the strains below the macro yield point are yet small, the material behavior is viscoelastic and the stretch field is uniform. During continued deformation, localized zone develops in the the center of the specimen and starts to extend towards the grips.

Even if the discretization of the mesh with the plane elements fails to present the deformed shape in the thickness direction, comparison of the EBPA model results in Figs. 6 and 7 indicates that the deformation mode has not marked influence either on the neck propagation or on the intensity of plastic stretching. The thickness reduction ratio t/t_0 in the middle of the specimen is also presented in Fig. 7. Early on necking $u/H = 0.15$, the observed and EBPA model results are virtually indistinguishable. Once the elongation of $u/H = 0.15$ is passed, the thickness reduction ratio tends asymptotically to the limit $t/t_0 = 0.85$.

In conclusion, the difference between the model calibrations for homogeneous and inhomogeneous deformation is not a result of the localization phenomena or volume changes shown in Fig.
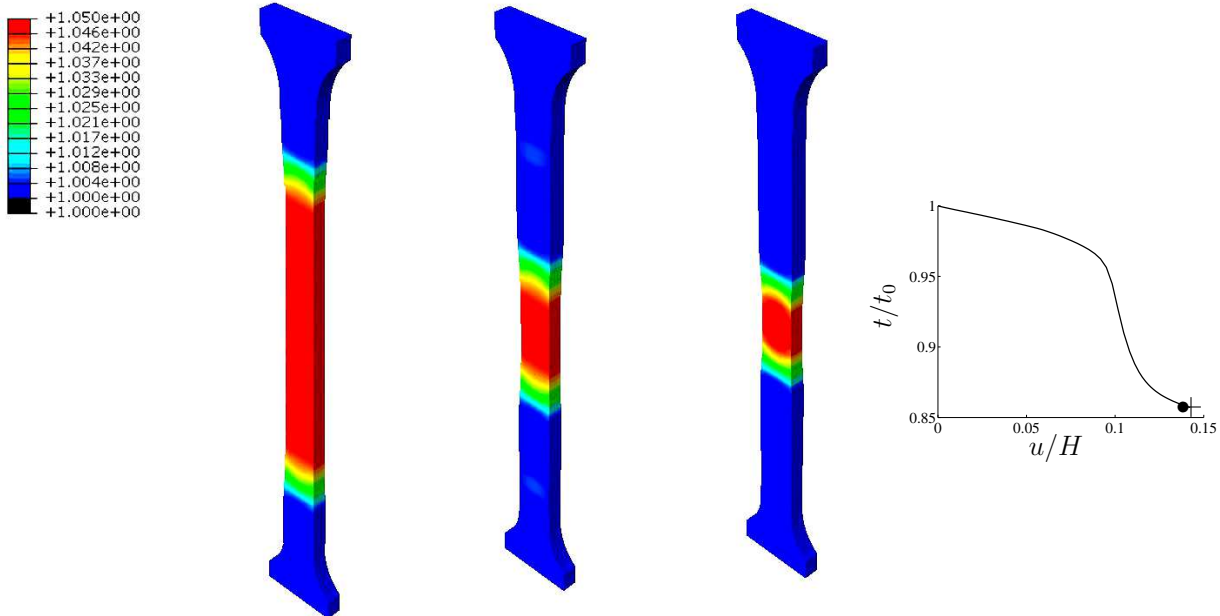
Figure 7: Based on a three-dimensional finite-element code of the EBPA model, the deformed shapes of the specimen during the stabilized neck, $u = 15$ mm, $u = 20$ mm and $u = 35$ mm, are visualized by $\bar{\lambda}_{ec}^{p}$. The thickness-reduction ratio t/t_0 at $x = 0$ and $y = (L + u)/2$ (right). The markers $\bullet$ and $+$ denote the thickness ratio according to the model and the experiment, respectively. The finite element discretization is of a mesh with 8-node linear hybrid brick elements.

7. Instead, the discrepancy is due to the EBPA model's ability to capture the time dependent (viscous) deformation behavior. The time dependent behavior is one consequence of the macro-molecular character of polymers, i.e. the polymer chains need a relaxation time to attain their equilibrium state after deformation. In order to find the mechanisms that are able to explain the discrepancy in more detail, several factors, such as the number of entanglements, possible disentanglement, void growth and crazing, are investigated and they are considered in a part of the EBPA model.

4 Investigation of the damage behavior

The objective of this section is to investigate the influence of damage on localized deformation behavior. In subsequent considerations, damage is ascribed to the distributed growth of void volume and crazing during plastic deformation. Here, the concept of free volume is employed to describe the voids or the loosely packed regions in the PC under consideration. In contrast to rubber-toughened polymers, the void is considered as conceptual with no clear physical interpretation. However, since the voids are uniformly distributed in the material, the growth of voids is approximated by using the models which are conventionally applied to the modeling of void growth due to cavitation of small rubber particles (second-phase particles) or impurities present in polymer-rubber blends. An example of these polymer blends is PC incorporating small polyacrylonitrile-butadiene-styrene (ABS) particles, cf. e.g. [19].

Due to the existence of voids around the chain molecules, the yield behavior of amorphous glassy polymers depends on hydrostatic pressure. The damage mechanism is schematically illustrated in Fig. 8. During nucleation and initial growth of voids, the deformation is considered as homogeneous. Once the voids have grown and the coalescence of voids is initialized, the transformation to the localized deformation phase takes place.
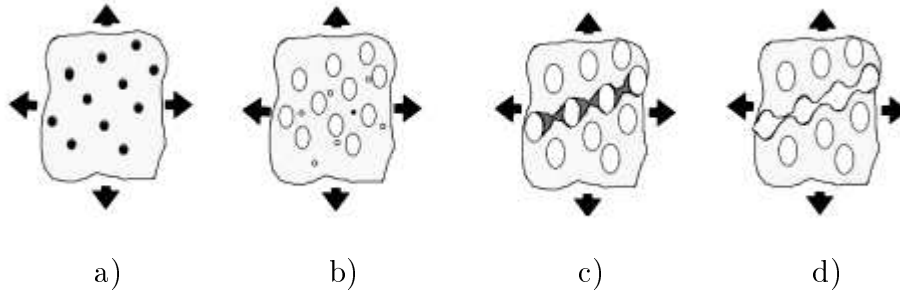
12

Figure 8: A schematic representation of the dilatational damage mechanism: a) nucleation of voids, b) void growth, c) initialization of void coalescence and d) the coalesced voids.

A widely used dilatational plasticity model is the one introduced by [25] and later modified by [26]. The Gurson model is based on the assumption that the deformation mode of the material surrounding a void is homogenous. According to this model, softening behavior in the material results from the growth of voids, i.e. the model does not possess the intrinsic ability to predict localized deformation by void coalescence. Due to a low initial void volume, the voids are assumed to become coalesced in very large strains, i.e. void growth is only ascribed to the nucleation of new voids instead of void coalescence.

4.1 Modeling of void growth

In order to investigate the damage behavior caused by void growth, macroscopic constitutive relations in the EBPA model are modified by using an augmented Gurson model, which also takes the nucleation of new voids into account.

Since the voids are assumed to be spherical in shape and uniformly distributed, the damage evolution is assumed to be isotropic and it is represented by a single scalar termed a void volume fraction $f_v = dV_v/dV$ having the initial value $0 \leq f_{v0} \leq f_v < 1$. The infinitesimal volume dV_v represents the volume change occupied by the voids and dV is the total volume change of the representative volume element (RVE). As with the Jacobian J, which is defined as the ratio of the current volume change dV and the initial volume change dV_0 as $J := dV/dV_0$, the void volume fraction can be represented as $J^v := dV/dV_m$, where $dV_m = dV - dV_v$ is the volume change occupied by the matrix material.

Since the inelastic Gurson potential Φ^p acts as both a yield function and a potential for plastic flow, the theory is considered as associative. To better predict the instability in the material due to the interaction of voids, [26] proposed a modified Gurson damage model in which the inelastic potential is given by

$$\Phi^p(\tau, f_v, \tau_m, \tau_e) = \tau^2 + 2f_v q_1 \tau_e^2 \cosh(\frac{3}{2}q_2\frac{\tau_m}{\tau_e}) - \tau_e^2(1 + q_1^2 f_v^2) \tag{28}$$

where $\tau_m := 1/3\mathrm{trace}(\boldsymbol{\tau})$ is the macroscopic mean stress. In accordance with the previous approaches by [26, 37], the microscopic effective stress of the solid ligaments τ_e is introduced separately from the macroscopic effective stress τ. The microscopic effective stress τ_e is determined from the condition $\Phi^p = 0$. Since the volumetric deformation is suppressed in the flow rule (20), it is generally inappropriate for modeling damage. Based on the potential (28), the rate of plastic deformation is governed by the modified normality rule

$$\boldsymbol{d}^p = \dot{\Lambda}^p \frac{\partial \Phi^p}{\partial \boldsymbol{\tau}} \tag{29}$$

13

which allows dilative plastic flow to be evolved in the material. The scalar valued parameter $\dot{\Lambda}^{\mathrm{p}}$ is defined below. The kinematic hardening effect is included in the model via the macroscopic effective stress $\tau(\tilde{\boldsymbol{\tau}})$, which was defined by (20). As with the BPA model, the intrinsic softening is modeled via the athermal shear strength s_1, which is taken to evolve according to $(26)_1$. The isotropic hardening effect is enforced by the internal variable s_2 given by $(26)_2$.

In contrast to the original Gurson spherical model for incompressible, rigid-plastic material, [26] suggested that the values $q_1 = q_2 = 1$ in (28) need to be replaced by $q_1 = 1.5$ and $q_2 = 1.0$ to better capture bifurcation away from the nominally homogeneous deformation. For amorphous glassy polymers, however, the constant values of q_1 and q_2 cannot satisfactorily predict either void growth or the change of the void shape during deformation. To capture the expected characteristics of void growth, [20] suggested that q_1 and q_2 should be considered as internal variables given by the following empirical power laws:

$$q_1 = q_{10}(1 + cp_{\mathrm{v}})^{N_{\mathrm{v}}}, \quad q_2 = q_{20}(1 + cp_{\mathrm{v}})^{N_{\mathrm{v}}} \tag{30}$$

where q_{10}, q_{20}, c and N_{v} are positive constitutive parameters and p_{v} denotes an internal variable defined subsequently. The low values of q_{10} and q_{20} indicate weak interactions between the voids while softening in the material decreases, cf. [20]. In the flow rule (29), a scalar parameter $\dot{\Lambda}^{\mathrm{p}}$ was introduced. This can be determined from equivalence between the plastic power which is dissipated into the porous media and into the corresponding solid ligaments between the voids, i.e.

$$\tilde{\boldsymbol{\tau}} : \boldsymbol{d}^{\mathrm{p}} = (1 - f_{\mathrm{v}})\sqrt{2}\tau_{\mathrm{e}}\dot{p}_{\mathrm{v}}. \tag{31}$$

In the equation (31), $\dot{p}_{\mathrm{v}}$ denotes the effective plastic strain rate, which is chosen to be equal to the plastic shear strain rate $\dot{\gamma}^{\mathrm{p}}$ given in (24). Since $\dot{\gamma}^{\mathrm{p}}$ is positive, γ^{p} is monotonically increasing and as a result the variables q_1 and q_2 given by (30) increase during deformation. It then follows from (29) and (31) that

$$\dot{\Lambda}^{\mathrm{p}} = \sqrt{2}(1 - f_{\mathrm{v}})\tau_{\mathrm{e}}\dot{\gamma}^{\mathrm{p}}(\tilde{\boldsymbol{\tau}} : \frac{\partial \Phi^{\mathrm{p}}}{\partial \boldsymbol{\tau}})^{-1}.$$

Based on the normality rule (29), the rate of plastic deformation takes the following form

$$\boldsymbol{d}^{\mathrm{p}} = \sqrt{2}(1 - f_{\mathrm{v}})\dot{\gamma}^{\mathrm{p}}\tau_{\mathrm{e}}(2\tau^2 + \Xi\mathrm{trace}(\tilde{\boldsymbol{\tau}}))^{-1}(\tilde{\boldsymbol{\tau}}^{\mathrm{dev}} + \Xi\boldsymbol{i}),$$
$$\Xi := q_1 q_2 f_{\mathrm{v}}\tau_{\mathrm{e}}\sinh\left(\frac{3}{2}q_2\frac{\tau_{\mathrm{m}}}{\tau_{\mathrm{e}}}\right). \tag{32}$$

It should be noticed that the condition $\Phi = 0$ yields $\tau_{\mathrm{e}} = \tau$ if $q_{10} = q_{20} = 0$, i.e. no interaction between the voids exists. Under this condition, a realistic assumption is that damage does not evolve, i.e. $\dot{f}_{\mathrm{v}} = 0$ and the normality rule (32) is equal with (20) for the plastic deformation through shear yielding.

The damage process due to the presence of voids can be separated into the two phases, cf. Fig. 8(a-b) and (c-d). First, the homogenous deformation takes place with void nucleation and initial growth, which is followed by the localized deformation due to continued void growth and void coalescence. Since void coalescence is neglected here, the evolution law for these two phases can additively be decomposed as

$$\dot{f}_{\mathrm{v}} = \dot{f}_{\mathrm{g}} + \dot{f}_{\mathrm{n}}, \quad f_{\mathrm{v}}(0) = f_{\mathrm{v0}} \tag{33}$$

where $\dot{f}_{\mathrm{g}}$ and f_{n} describe the growth of existing voids and the nucleation of new voids, respectively. To define their evolution laws, let us first consider the void volume fraction only due to growth of existing voids defined as $f_{\mathrm{g}} = dV_{\mathrm{g}}/dV$. The initial value ranges between $0 \le f_{\mathrm{g0}} \le f_{\mathrm{g}} < 1$. As with the volume fraction J^{v}, the void volume fraction due to growth of existing voids can be

represented as $J^{\mathrm{g}} := dV/dV_{\mathrm{mg}}$, where $dV_{\mathrm{mg}} = dV - dV_{\mathrm{g}}$ is the volume change occupied by the matrix material due to growth of existing voids. The relation between J^{g} and f_{g} becomes

$$f_{\mathrm{g}} = 1 - \frac{1}{J^{\mathrm{g}}}. \tag{34}$$

Taking note of (34), lead us to the following evolution equation

$$\overline{\ln J^{\mathrm{g}}} = \frac{\dot{J}^{\mathrm{g}}}{J^{\mathrm{g}}} = \frac{\dot{f}_{\mathrm{g}}}{1 - f_{\mathrm{g}}}. \tag{35}$$

Assuming also that void growth takes place only due to the plastic deformation, i.e. $J^{\mathrm{g}} = J^{\mathrm{p}}$ in (35), and applying Liouville's theorem to $\boldsymbol{F}^{\mathrm{p}}$ yield

$$\dot{f}_{\mathrm{g}} = 3(1 - f_{\mathrm{g}})D_{\mathrm{h}}^{\mathrm{p}}. \tag{36}$$

In the evolution equation (36), $D_{\mathrm{h}}^{\mathrm{p}} := 1/3\mathrm{trace}(\boldsymbol{d}^{\mathrm{p}})$ is the plastic volumetric strain rate, cf. [25].

In many amorphous glassy polymers, the nucleation of new voids is also assumed to be significant but the process is not well understood yet. It is a material intrinsic property being dependent on the strength of the polymeric material as well as on the size and shape of existing voids. Large voids usually nucleate new voids earlier than small voids, and inclusions with different length scales may also lead to different nucleation criteria, cf. [38]. To capture the accelerated damage due to the nucleation of new voids, [39] proposed the following strain-controlled law for the nucleation rate

$$\dot{f}_{\mathrm{n}} = \frac{f_{\mathrm{N}}}{s_{\mathrm{v}}\sqrt{2\pi}} \exp\left(-\frac{1}{2}\left(\frac{\gamma^{\mathrm{p}} - \varepsilon_{\mathrm{N}}}{s_{\mathrm{v}}}\right)^2\right)\dot{\gamma}^{\mathrm{p}} \tag{37}$$

where f_{N} is a material parameter. The mean value ε_{N} of the normal distribution describes the critical strain beyond which the first new voids appear. Since not all the inclusions or particles will nucleate new voids, the parameters f_{N}, ε_{N} and the standard deviation s_{v} are averagely determined from calibration to the material's macroscopic response.

One important aspect is the ability of the proposed model to account for the real deformation behavior as well as quantitative damage prediction. For the numerical evaluation of the model, it is implemented in a finite element program and the constitutive equations (17) and (26) are completed by the integration of the void volume fraction rates given by (36) and (37). It should be noticed that the plastic shear γ^{p}, which is needed in (37), is available from the solution of the hardening variable s_2, cf. (26). Moreover, the rate of plastic deformation is governed by the normality rule (32). The numerical treatment of the model is discussed in Appendix A.

Thermodynamics

Based on the multiplicative splits (1) and (15) and the existence of the field variable J^{v} thermodynamical treatment of the proposed model is presented, cf. [34, 40]. Without loss of generality, the considerations are presented in the spatial configuration. Assuming isothermal conditions to prevail, thermomechanical potential φ, also called Helmholz' free energy per unit volume, is given by

$$\varphi = \hat{\varphi}(\boldsymbol{b}_1^{\mathrm{e}}, \bar{\boldsymbol{C}}^{\mathrm{p}}, J^{\mathrm{v}}, \psi) = \varphi^{\mathrm{e}}(\boldsymbol{b}_1^{\mathrm{e}}, J^{\mathrm{v}}) + \varphi^{\mathrm{p}}(\bar{\boldsymbol{C}}^{\mathrm{p}}) + \psi(\boldsymbol{b}_2^{\mathrm{e}}) \tag{38}$$

where φ^{e} and φ^{p} are the elastic and the plastic part of the free energy, respectively, and the potential ψ is defined subsequently. The plastic deformation tensor $\bar{\boldsymbol{C}}^{\mathrm{p}}$ was defined by (8),

$$\boldsymbol{b}_2^{\mathrm{e}} := \boldsymbol{F}_2^{\mathrm{e}}\boldsymbol{F}_2^{\mathrm{e,T}} = (\boldsymbol{v}_2^{\mathrm{e}})^2 \quad \text{and} \quad \boldsymbol{b}_1^{\mathrm{e}} := \boldsymbol{F}_1^{\mathrm{e}}\boldsymbol{F}_1^{\mathrm{e,T}} = (\boldsymbol{v}_1^{\mathrm{e}})^2 \tag{39}$$

is the elastic deformation tensor. To derive the constitutive relations for the stresses, advantage are taken of the developments by [41, 42]. Taking the symmetric part of (3) and considering the product decomposition (15) yields

$$\boldsymbol{d} = \boldsymbol{d}^{\mathrm{e}} + \boldsymbol{d}^{\mathrm{p}} = \boldsymbol{d}_1^{\mathrm{e}} + \boldsymbol{d}_2^{\mathrm{e}} + \boldsymbol{d}^{\mathrm{p}} \tag{40}$$

where

$$\boldsymbol{d}_1^{\mathrm{e}} := \mathrm{sym}(\dot{\boldsymbol{F}}_1^{\mathrm{e}} \boldsymbol{F}_1^{\mathrm{e}-1}), \quad \boldsymbol{d}_2^{\mathrm{e}} := \mathrm{sym}(\boldsymbol{F}_1^{\mathrm{e}} \bar{\boldsymbol{l}}_2^{\mathrm{e}} \boldsymbol{F}_1^{\mathrm{e}-1})$$

and

$$\bar{\boldsymbol{l}}_2^{\mathrm{e}} := \dot{\boldsymbol{F}}_2^{\mathrm{e}} \boldsymbol{F}_2^{\mathrm{e}-1}. \tag{41}$$

In terms of the internal power $\mathfrak{W}^{\mathrm{int}}$ and the rate of the free energy $\dot{\varphi}$, the dissipation per unit volume in the spatial configuration is governed by

$$\mathcal{D} = \mathfrak{W}^{\mathrm{int}} - \dot{\varphi} := \boldsymbol{\tau} : \boldsymbol{d}_1^{\mathrm{e}} + \boldsymbol{\tau} : \boldsymbol{d}_2^{\mathrm{e}} + \boldsymbol{\tau}^{\mathrm{p}} : \boldsymbol{d}^{\mathrm{p}} + \frac{1}{3}\mathrm{trace}(\boldsymbol{\tau}^{\mathrm{v}})\overline{\ln J^{\mathrm{v}}} - \dot{\varphi} \geq 0 \tag{42}$$

where $\mathrm{trace}(\boldsymbol{\tau}^{\mathrm{v}})$ and $\boldsymbol{\tau}^{\mathrm{p}}$ represent the internal microstresses work conjugate to $\overline{\ln J^{\mathrm{v}}}$ and $\boldsymbol{d}^{\mathrm{p}}$, respectively. Specifically, $\mathrm{trace}(\boldsymbol{\tau}^{\mathrm{v}})$ is the mean stress needed to reach the volume change due to void growth, i.e. it differs from the microscopic effective stress τ^{e} of the solid ligaments between the voids. The rate of the free energy $\dot{\varphi}$ in (42) becomes

$$-\dot{\varphi}(\boldsymbol{b}_1^{\mathrm{e}}, \bar{\boldsymbol{C}}^{\mathrm{p}}, J^{\mathrm{v}}, \psi) = -\frac{\partial \varphi^{\mathrm{e}}(\boldsymbol{b}_1^{\mathrm{e}})}{\partial \boldsymbol{b}_1^{\mathrm{e}}} : \dot{\boldsymbol{b}}_1^{\mathrm{e}} - \frac{\partial \varphi^{\mathrm{p}}(\bar{\boldsymbol{C}}^{\mathrm{p}})}{\partial \bar{\boldsymbol{C}}^{\mathrm{p}}} : \dot{\bar{\boldsymbol{C}}}^{\mathrm{p}} - J^{\mathrm{v}}\frac{\partial \varphi^{\mathrm{e}}(J^{\mathrm{v}})}{\partial J^{\mathrm{v}}}\overline{\ln J^{\mathrm{v}}} - \dot{\psi} \tag{43}$$

where $\dot{\psi} := \boldsymbol{\tau}_2 : \boldsymbol{d}_2^{\mathrm{e}}$. Taking advantage of (11) and noting the free energy being isotropic tensor function of $\boldsymbol{b}_1^{\mathrm{e}}$ lead us to the following expression

$$\frac{\partial \varphi^{\mathrm{e}}}{\partial \boldsymbol{b}_1^{\mathrm{e}}} : \dot{\boldsymbol{b}}_1^{\mathrm{e}} = 2\frac{\partial \varphi^{\mathrm{e}}}{\partial \boldsymbol{b}_1^{\mathrm{e}}}\boldsymbol{b}_1^{\mathrm{e}} : \boldsymbol{d}_1^{\mathrm{e}}, \tag{44}$$

cf. e.g. [43]. Applying (9) and assuming that the plastic part of the free energy is an isotropic function of $\bar{\boldsymbol{C}}^{\mathrm{p}}$ gives

$$\frac{\partial \varphi^{\mathrm{p}}}{\partial \bar{\boldsymbol{C}}^{\mathrm{p}}} : \dot{\bar{\boldsymbol{C}}}^{\mathrm{p}} = 2\mathrm{sym}(\frac{\partial \varphi^{\mathrm{p}}}{\partial \bar{\boldsymbol{C}}^{\mathrm{p}}}\bar{\boldsymbol{C}}^{\mathrm{p}}) : \bar{\boldsymbol{D}}^{\mathrm{p}} =: \bar{\boldsymbol{B}} : \bar{\boldsymbol{D}}^{\mathrm{p}} \tag{45}$$

where the principal components of the backstress $\bar{\boldsymbol{B}}$ in the intermediate configuration are defined as

$$\bar{B}_\alpha := \frac{C_{\mathrm{R}}}{3\lambda_{\mathrm{ec}}^{\mathrm{p}}}\sqrt{N}\mathfrak{L}^{-1}(\frac{\lambda_{\mathrm{ec}}^{\mathrm{p}}}{\sqrt{N}})(\bar{\lambda}_\alpha^{\mathrm{p}})^2, \quad \alpha = 1, 2, 3, \tag{46}$$

cf. (23). The plastic part of the free energy φ^{p} and a detailed account to obtain the backstress, which equals with equation (46), can be found e.g. from [36]. In the present models, the backstress represents the non-dissipative stress, i.e. a part of the plastic work which is stored in the material during deformations. Substituting (44) and (45) into the dissipation inequality (42) yields

$$\mathcal{D} := \left(\boldsymbol{\tau} - 2\frac{\partial \varphi^{\mathrm{e}}}{\partial \boldsymbol{b}_1^{\mathrm{e}}}\boldsymbol{b}_1^{\mathrm{e}}\right) : \boldsymbol{d}_1^{\mathrm{e}} + (\boldsymbol{\tau} - \boldsymbol{\tau}_2) : \boldsymbol{d}_2^{\mathrm{e}} + (\boldsymbol{\tau}^{\mathrm{p}} - \boldsymbol{\beta}) : \boldsymbol{d}^{\mathrm{p}} + (\frac{1}{3}\mathrm{trace}(\boldsymbol{\tau}^{\mathrm{v}}) - J^{\mathrm{v}}\frac{\partial \varphi^{\mathrm{e}}(J^{\mathrm{v}})}{\partial J^{\mathrm{v}}})\overline{\ln J^{\mathrm{v}}} \geq 0 \tag{47}$$

where $\boldsymbol{\beta}$ is the backstress expressed in the spatial configuration. Using the arguments by [44] turns out the following expressions

$$\boldsymbol{\tau} = 2\frac{\partial \varphi^{\mathrm{e}}}{\partial \boldsymbol{b}_1^{\mathrm{e}}}\boldsymbol{b}_1^{\mathrm{e}} \tag{48}$$

16

and

$$\text{trace}(\boldsymbol{\tau}^{\text{v}}) = 3J^{\text{v}} \frac{\partial \varphi^{\text{e}}(J^{\text{v}})}{\partial J^{\text{v}}} \tag{49}$$

for the stress and the microstress, respectively. Consistent with the internal power $\mathfrak{W}^{\text{int}}$, $\boldsymbol{d}_2^{\text{e}}$ appears linearly in (47) and thus $\boldsymbol{\tau}_2 = \boldsymbol{\tau}$. Taking advantage of (48), the local dissipation (47) reduces to

$$\mathcal{D} := \tilde{\boldsymbol{\tau}} : \boldsymbol{d}^{\text{p}} \geq 0, \quad \tilde{\boldsymbol{\tau}} := \boldsymbol{\tau}^{\text{p}} - \boldsymbol{\beta} \tag{50}$$

where $\tilde{\boldsymbol{\tau}}$ is the thermodynamic driving stress.

Assuming the choice $\boldsymbol{\tau}^{\text{p}} := \boldsymbol{\tau}$ satisfies the condition (50). Since $\dot{\gamma}^{\text{p}}$ is positive, also the microstress of the ligaments τ_{e} must be positive in (31). However, this condition must be handled with care, since it is not generally satisfied by the solution of $\Phi^{\text{p}} = 0$, cf. (28).

Since the polymer chains in the EBPA model are assumed to be randomly oriented in space, use is made of an isotropic strain energy,

$$\varphi = \frac{1}{2} \kappa (I_1^{\text{e}})^2 + 2\mu J_2^{\text{e}}, \tag{51}$$

where κ and μ are the bulk and shear modulus, respectively. The logarithmic invariants needed in Eq. (51) are defined as

$$I_1^{\text{e}} := \text{trace}(\ln \boldsymbol{v}_1^{\text{e}}) = \ln J_1^{\text{e}} \quad \text{and} \quad J_2^{\text{e}} := 1/2 (\ln \boldsymbol{v}_1^{\text{e}})^{\text{dev}} : (\ln \boldsymbol{v}_1^{\text{e}})^{\text{dev}}.$$

Using the specific strain energy (51) in (48), the Kirchhoff stress takes the following form

$$\boldsymbol{\tau} = 2\mu (\ln \boldsymbol{v}_1^{\text{e}})^{\text{dev}} + \kappa \ln J_1^{\text{e}} \boldsymbol{i} =: \boldsymbol{\mathcal{L}}^{\text{e}} : \ln \boldsymbol{v}_1^{\text{e}} \tag{52}$$

where $\boldsymbol{\mathcal{L}}^{\text{e}}$ was defined in (18). Similar to (34), a relation between the void volume fraction f_{v} and J^{v} can be derived. In analogy with (35), the evolution equation for $d(\ln J^{\text{v}})/dt$ in terms of $\dot{f}_{\text{v}}$ can be expressed, i.e. both void growth and shrinkage are allowed without the thermodynamics being violated. Also, the dependence of the strain energy (51) on J^{v} through the elastic constitutive parameters κ and μ can be defined. Several possible models can be found for the dependence of κ and μ on f_{v}, cf. e.g. [45, 46].

4.2 Calibration and evaluation of the augmented EBPA model for void growth

The augmented Gurson model in conjunction with the EBPA model is calibrated to data obtained from the cold drawing experiment. In the calibration, the finite element discretization is of a mesh with 196 4-node plane elements, i.e. the same element mesh as before is employed. It can be assumed that the void volume fraction has only a small influence on the elastic material properties in porous media, cf. [46], and thus the elastic constitutive parameters are considered as constant. Concerning damage, the calibration is initialized using the parameters for rubber-toughened PMMA (RTPMMA) taken from [20]. Both the calibrated and the parameters for RTPMMA are listed in Table 4. In the subsequent simulations, the localization is triggered according to (27) using $\xi_0 = 0.002$. Calibration also indicated that

- the growth of void volume suppresses the isotropic softening effect,
- the change in the initial void volume fraction from $f_{\text{v0}} = 0$ to $f_{\text{v0}} = 0.05$ only has a small effect on the macroscopic $f - u$ response,
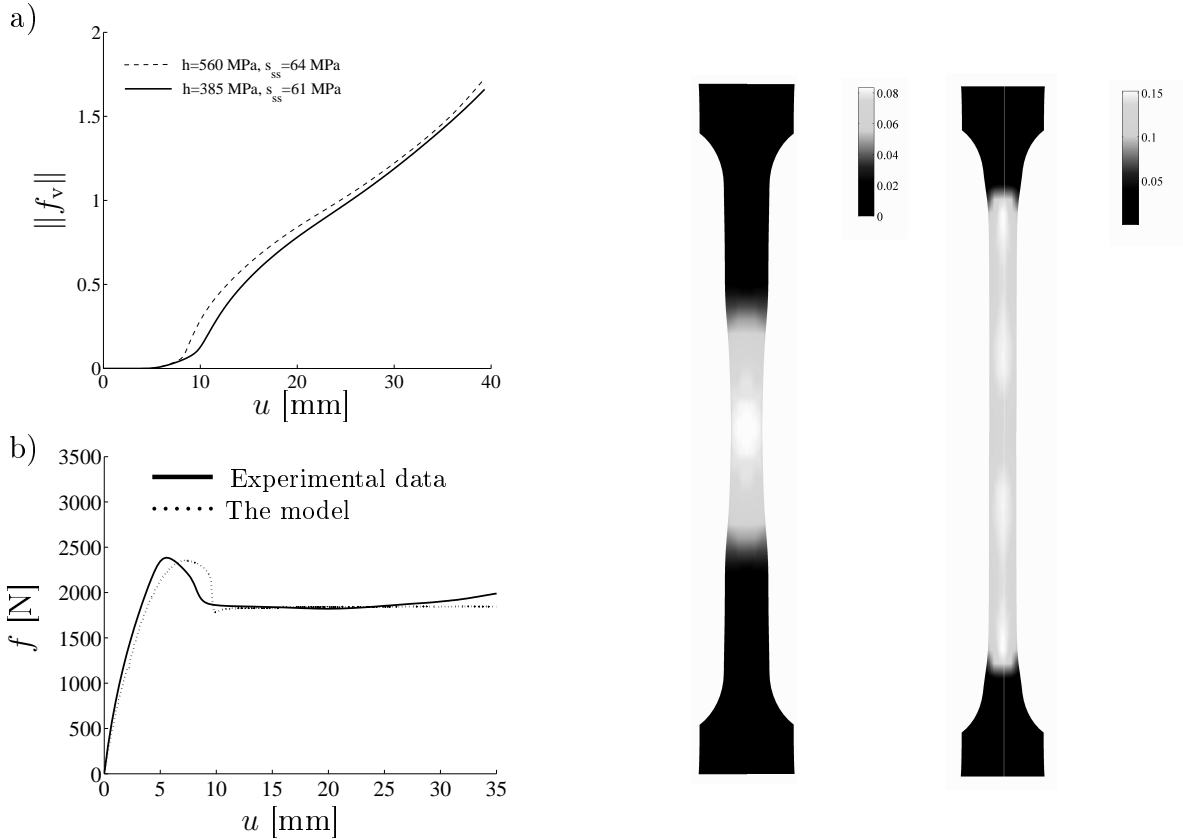
Figure 9: a) Influence of the parameter h_1 on void growth, which is represented by the norm of void volume fraction $\|f_{\mathrm{v}}\| := \sqrt{\sum_i (f_{\mathrm{v},i} \cdot f_{\mathrm{v},i})}$ where $f_{\mathrm{v},i}$ are the extrapolated values of void volume fraction at the nodes of the mesh. b) $f - u$ responses according to the test and the model. The deformed shapes at $u = 20$ mm and at the end of loading are visualized by void volume fraction f_{v}. The highest porosity f_{v} is highlighted in white.

- the values $c > 0$, which influence damage evolution via (30), reduce void growth.

Since the PC polymer under study is not interspersed by small rubber particles, and the influence of a low initial void volume fraction on the macroscopic response is negligible, we set $f_{\mathrm{v}0} = 0$.

Fig. 9 presents the total growth of void volume and the influence of the hardening slope h_1 on the void growth. The values ranging between $385 - 560$ MPa are seen to have only a minor effect on void growth and thus the minimum value will be used in further considerations. Fig. 9 shows also the force vs elongation response according to both the test and the EBPA model. Even if the responses deviate during the softening phase, the model is well able to capture the initiation and stabilization of neck. Comparison of Figs. 9(a-b) reveals that the void nucleation is

Table 4: Constitutive parameters of the damage model for RTPMMA and PC. Calibration of the proposed model is performed to data obtained from the cold drawing experiment on PC. The RTPMMA parameters are taken from [20].

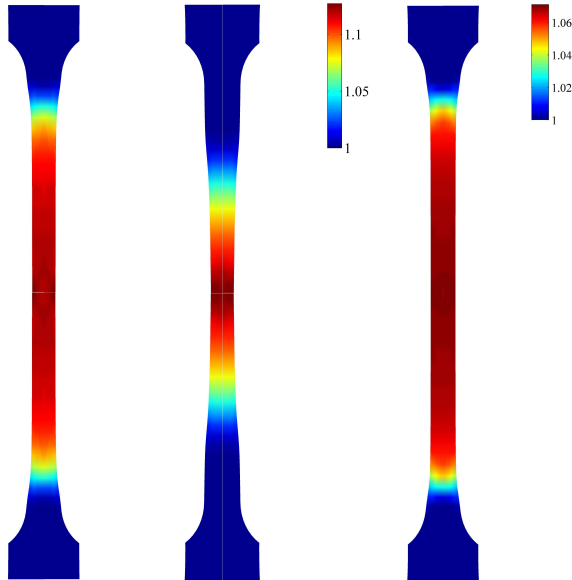|	η	h_1	s_{ss}	ε_{N}	s_{v}	f_{N}	q_{10}	q_{20}	c	N_{v}
	MPas	MPa	MPa							
RTPMMA				0.03	0.15	0.15	0.9	1.2	0.2	1.5
EBPA for PC	$1.5 \cdot 10^5$	385	61	0.03	0.15	0.05	1.5	1.0	0.2	1.5

Figure 10: Distribution of the plastic stretch $\bar{\lambda}_{ec}^{p}$ at the end of loading ($u = 40$ mm) according to the BPA model (on the left), the EBPA model and the EBPA model in conjunction with the damage model (on the right). The simulation based on the damage model is performed using the calibrated material parameters given in Table 4.

prohibited until the elongation $u \approx 6$ mm is reached. This threshold corresponds approximately to the elongation prior to the yield drop. Once the yield point in the stress response is passed, void growth develops and increases the porosity in the localized zone. During stabilized neck, voids grow rapidly in the material. Similar to the plastic stretching, the highest values appear in a region which gradually expands from the center of the specimen towards the grips during elongation. At the end of loading, the porous region covers the gauge section entirely, and the highest porosity occurs in the two separate regions beyond the mid-plane, $y = (L + u)/2$.

Having less intrinsic softening due to void growth allows the softening slope h_1 and the intensity s_{ss}/s_0 to be reduced to a level which agrees more closely with the values obtained from the calibration for homogeneous deformation, cf. Table 2. As a consequence, the intensity $s_{ss}/s_0 = 0.80$, which appears in Table 3 and was previously employed in the EBPA model, is reduced to 0.65. Moreover, the value $h_1 = 385$ MPa is virtually two times lower compared to its preceding value in Table 3. It can be concluded that the difference between the calibrations for homogeneous and inhomogeneous deformation is strongly affected by void growth in the material.

Based on the model simulations the plastic stretch distributions are highlighted in Fig. 10. It can be observed that damage reduces the intensity of the plastic stretching, while the localized deformation expands more rapidly along the specimen. A glance at Fig. 6 reveals that the necked region, which is predicted by the combined EBPA and the damage model, reaches the end of the gauge section simultaneously with the experiment. Assuming the localization of plastic stretching is representative for the evolution of shear banding, the kinematic hardening, which is enforced by void growth, is seen to promote localization through widening of shear bands.

As has been shown, the EBPA model, along with the augmented Gurson model for void growth, is able to predict the transformation from the homogeneous deformation phase to the localized deformation phase well. Applying this model, the difference between the model parameters, which result from the calibration for homogeneous and inhomogeneous deformation, also decreased considerably. A shortcoming of the model is that the force-elongation response during

neck shows a premature hardening while the void volume fraction grows and attains values too high for unvoided polymers.

4.3 Modeling of crazing

Under compression, amorphous polymers show ductile localized deformation behavior, which is due to shear yielding without marked volume changes. In contrast to the shear yielding mechanism, which eventually leads to fracture by a chain scission, the governing mechanism of inelastic deformation under tension is crazing, cf. [5, 6]. More precisely, crazing is assumed to result from disentanglement in highly concentrated regions of maximum principal stress. Disentanglement nucleates new micro-voids which grow and coalesce to form initial crazes and cause stretching and eventually failure of the thin fibrils between the two faces of the initial crazes, cf. [14, 47]. As a result of the breakdown of the fibrils, crazes widen leading to local brittle failure while material behavior at the macroscopic level still shows a little ductility. In all, the nominally brittle failure can be separated into the three different phases: craze-initiation, widening and craze-breakdown.

In recent years, cohesive-surface models have been widely applied to the numerical simulation of craze-initiation, growth and breakdown with the finite element method, cf. e.g. [13, 19]. In a finite element setting, however, cohesive interface approaches allow for the nucleation and growth of the crack only along the element boundaries. In order to avoid mesh dependence and priori assumptions concerning the orientation of interface elements for crazing, an alternative, continuum-based model is proposed here. Based on the work by [5], a simple craze-initiation criterion is introduced and the transition from shear-flow to craze-flow is carried out by a change of the flow rule, where the inelastic deformation is taken to occur in the direction of the local maximum principal stress. Once the local critical plastic strain is reached, crazes rapidly widen which eventually leads to local fracture or chain-breakdown under compression or tension, respectively.

The craze-initiation can be governed by strain- or stress-based criteria. [48] conducted tension-torsion stress-controlled experiments on thin-walled tubular specimens, which indicated that there is a time delay between the application of stress and the first appearance of crazing. At the stress levels, where the equivalent stress τ and the mean normal stress τ_m exceed 0.4 - 0.5 of the yield stress, the delay time considerable decreases and as a result craze-initiation can be considered as instantaneous event. Since the crazing process in the present drawing experiments occurs in stress levels higher than 0.4 - 0.5 of the yield stress, the incubation time for craze-initiation can be assumed negligible and a time-independent criterion can be applied in the proposed model.

In general, the development of crazing may be expected to have directional properties. Based on the assumption that the crazes grow in the direction of the maximum principal tensile stress, [5] proposed that crazing initiates when the mean stress is positive $\tau_m > 0$, and the highest principal stress τ_1 reaches a τ_m-dependent critical value $\tau_1 = \tau^{cr}(\tau_m) > 0$. They estimated the critical value τ^{cr} from the tension experiments on a smooth-bar, notched-bar and a compact tension specimen. They observed that the curve for craze-initiation just prior to the yield-peak load is reasonably-well captured by the function

$$\tau^{cr} = c_1 + \frac{c_2}{\tau_m} \tag{53}$$

where c_1 and c_2 are positive parameters. In general, stress-based criteria may be difficult to define with precision from experiments due to inaccuracies in controlling local stress states and the sites of craze-initiation, cf. [48]. For this reason, a corresponding strain-based criterion needs to be determined. It can be assumed that the crazes are initiated if the following two conditions are satisfied:

[1.] The highest principal tensile stress and the mean normal stress are positive, i.e. $\tau_1 > 0$ and $\tau_{\mathrm{m}} > 0$,

[2.] the craze-strain ζ^{P}, which evolves in the direction of the highest principal tensile stress, reaches a critical value $\zeta^{\mathrm{P}} := \int \dot{\zeta}^{\mathrm{P}} \mathrm{d}t = \zeta_{\mathrm{cr}}^{\mathrm{P}} > 0$. Correspondingly, $\tau_1 = \tau^{\mathrm{cr}} > 0$.

Once crazing has been initiated, the transition from shear-flow to craze-flow takes place while the plastic flow aligns with the direction of the maximum principal stress τ_1, and the inelastic deformation begins to evolve through widening of the crazes.

Instead of attempting to represent a detailed scheme for craze-widening, cf. [12, 13], a continuum-based model, which defines the inelastic deformation as an average over a microstructural representative volume element, is proposed. It is assumed that the material element contains enough plate-like craze regions that allow for macroscopically smooth craze-widening process prior to failure. The magnitude of the craze-flow is given by the macroscopic tensile craze-strain rate $\dot{\zeta}^{\mathrm{P}}$ and it evolves as long as τ_1 is positive. Following [49], $\dot{\zeta}^{\mathrm{P}}$ is assumed to be accounted for by the thickening rate $\dot{\delta}$ of the active planar crazes which are separated by an average spacing L_0, cf. Fig. 11. Thus the average tensile craze-strain rate becomes $\dot{\zeta}^{\mathrm{P}} = \dot{\delta}/L_0$. In terms of the eigenvectors $\boldsymbol{n}_1$ associated with the highest principal stress, the transition from shear-flow to craze-flow is given by
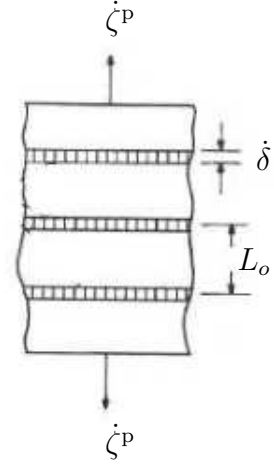

Figure 11: Widening of crazes at an average spacing L_0. The macroscopic tensile craze strain rate $\dot{\zeta}^{\mathrm{P}}$ is determined by the thickening rate $\dot{\delta}$ of crazes.

$$\boldsymbol{d}^{\mathrm{P}} = \begin{cases} \dot{\zeta}^{\mathrm{P}} \boldsymbol{n}_1 \otimes \boldsymbol{n}_1 & \text{if the conditions [1]-[2] are satisfied,} \\ \dot{\Lambda}^{\mathrm{P}}(\tilde{\boldsymbol{\tau}}^{\mathrm{dev}} + \Xi \boldsymbol{i}) & \text{otherwise} \end{cases} \tag{54}$$

where $\dot{\Lambda}^{\mathrm{P}} := \sqrt{2}(1-f_{\mathrm{v}})\dot{\gamma}^{\mathrm{P}}\tau_{\mathrm{e}}(2\tau^2 + \Xi\operatorname{trace}(\tilde{\boldsymbol{\tau}}))^{-1}$ and $\Xi := q_1 q_2 f_{\mathrm{v}} \tau_{\mathrm{e}} \sinh\big(3/2q_2 \tau_{\mathrm{m}}/\tau_{\mathrm{e}}\big)$, cf. (32). The magnitude of the rate of plastic deformation $\dot{\zeta}^{\mathrm{P}} = |\boldsymbol{d}^{\mathrm{P}}|$ is determined such that some continuity during the transition from shear-flow to craze-flow is ensured.

The equality between the plastic work rate in the porous material per unit volume and the dissipation in the matrix material is governed by

$$\tilde{\boldsymbol{\tau}} : \boldsymbol{d}^{\mathrm{P}} = (1 - f_{\mathrm{v}})\sqrt{2}\tau_{\mathrm{e}}\dot{\gamma}^{\mathrm{P}*}(\frac{\tau_1}{\tau_1^*})^m \tag{55}$$

where the quantities with the superscript ($*$) are determined at the instant when the change in the flow rule is triggered. It then follows from (37) that nucleation of new voids is governed by the constant rate $\dot{\gamma}^{\mathrm{P}*}$ during crazing. Since the experiments show an increased craze widening velocity with the applied stress intensity, cf. e.g. [13], the plastic work rate is reformulated in terms of the stress ratio τ_1/τ_1^*. The parameter m in (55) is found from the calibration to the experimental data. During shear flow, the stress ratio τ_1/τ_1^* remains unity and the plastic shear strain rate $\dot{\gamma}^{\mathrm{P}}$ evolves according to (24), i.e. (55) equals with (31). It follows from (54) and (55) that the magnitude $\dot{\zeta}^{\mathrm{P}} = |\boldsymbol{d}^{\mathrm{P}}|$ is given by

$$\dot{\zeta}^{\mathrm{P}} = \sqrt{2}(1 - f_{\mathrm{v}})\tau_{\mathrm{e}}\dot{\gamma}^{\mathrm{P}*}(\frac{\tau_1}{\tau_1^*})^m(\tilde{\boldsymbol{\tau}} : \boldsymbol{n}_1 \otimes \boldsymbol{n}_1)^{-1}. \tag{56}$$

The microscopic effective stress τ_e of ligaments is determined from the potential $\Phi^p = 0$, which for the craze-flow is modified such that the flow becomes oriented in the direction of the highest principal stress, i.e.

$$\Phi^p(\tau_1, f_v, \tau_e) = \frac{\tau_1^2}{2} + 2 f_v q_1 \tau_e^2 \cosh\left(\frac{q_2}{2} \frac{\tau_1}{\tau_e}\right) - \tau_e^2 (1 + q_1^2 f_v^2). \tag{57}$$
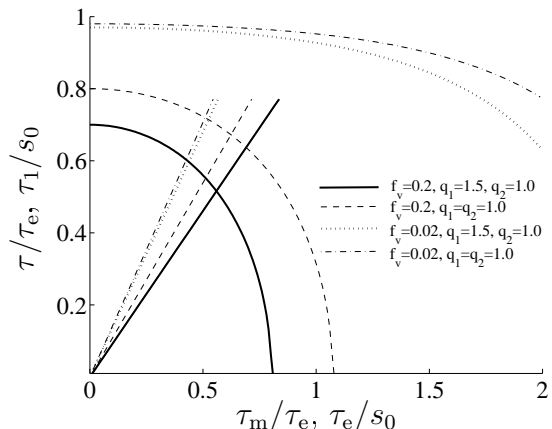

Figure 12: The potentials (28) and (57) in $\tau - \tau_m$ and $\tau_1 - \tau_e$ space, respectively. The influence of the two different values $f_v = 0.02$, $f_v = 0.2$ and $q_1 = 1.0$, $q_1 = 1.5$ are investigated.

Alternatively, employing the function (57) in the flow rule (29) (replacing $\dot{\Lambda}^p$ by $\dot{\zeta}^p$) and taking advantage of $\partial \tau_1 / \partial \boldsymbol{\tau} = \boldsymbol{n}_1 \otimes \boldsymbol{n}_1$ also results in the craze-flow rule (54), where $\dot{\zeta}^p$ is given by (56). Fig. 12 presents the potentials in (28) and (57) for different values of f_v and q_1. The stress trajectories in $\tau_1 - \tau_e$ space show proportionality between the macroscopic principal stressing and the microscopic stress in ligaments between the voids.

Since the final craze-breakdown can be considered as a physically unclear process, cf. [12, 13], a simple criterion for craze-breakdown and fracture are proposed as a first attempt. Following [5], the craze-breakdown under condition $\tau_1 > 0$ occurs when the local craze-strain ζ^p reaches a threshold value $\zeta_t^p > \zeta_{cr}^p > 0$. The threshold ζ_t^p in relation to the craze-initiation criteria $\zeta^p = \zeta_{cr}^p$ defines the length of the crazing process. In the situations where $\tau_1 \leq 0$, ductile fracture by molecular chain-scission is initialized as the plastic stretch $\bar{\lambda}_{ec}^p$ reaches a threshold $\bar{\lambda}_t^p$.

4.4 Calibration and evaluation of the augmented EBPA model for void growth and crazing

Based on the simulations of the cold drawing experiment the influence of crazing on the overall load-elongation response and localized deformation behavior is evaluated. In the simulations, the same element mesh as before is employed. Since the stretching in relation to the limiting stretch $\sqrt{N}$ in a representative volume element can be regarded as small during the entire cold drawing process, craze-breakdown barely initiates and will be neglected in the subsequent numerical simulations. Due to necking, the stress ratio τ_1/τ_1^* in (56) remains almost unaltered (near unity) during elongation and thus the parameter m is chosen to vanish.

Based on the discussion above, cf. also [9], the plastic deformation in large strains evolves primarily due to crazing and typically shows an increased rate of evolution once crazing has been initialized in the material. Since the stress level decreases during the crazing process, the plastic work rate in the porous material and the dissipation in the matrix material decrease, and as a result, the void volume fraction tends to increase, cf. (55). This effect is shown in Fig. 13. To exclude the integration of ζ^p, the corresponding stress criterion $\tau^{cr} = 62$ MPa for craze-initiation can be employed in the simulations. This threshold as well as the values $\bar{\lambda}_{ec}^p = 1.05 - 1.12$ in Fig. 13 for craze-initiation are reasonable-well captured by using the parameters $c_1 = 36$ MPa and $c_2 = 650$ MPa^2 in (53).
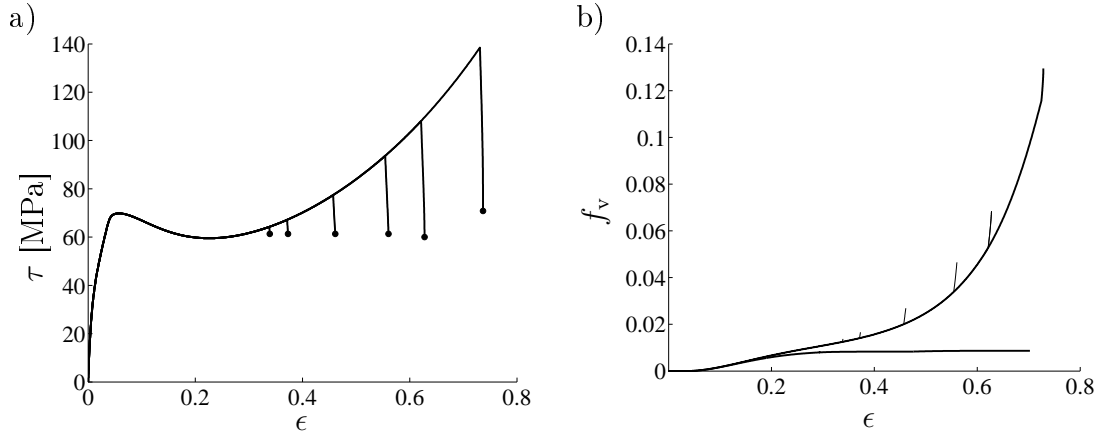
Figure 13: a) True stress vs true strain and b) void volume fraction for uniaxial tension of BPA-PC according to the model. Craze-initiation is prescribed by the plastic stretch at $\bar{\lambda}_{ec}^{P} = 1.04$, $\bar{\lambda}_{ec}^{P} = 1.05$, $\bar{\lambda}_{ec}^{P} = 1.08$, $\bar{\lambda}_{ec}^{P} = 1.12$, $\bar{\lambda}_{ec}^{P} = 1.15$ and $\bar{\lambda}_{ec}^{P} = 1.20$. In b), the curve involving a plateau represents void nucleation ($f_g = 0$) being virtually independent on craze-initiation. The simulation covers the time period of 750 s at $\dot{\epsilon} = 0.001$ 1/s.
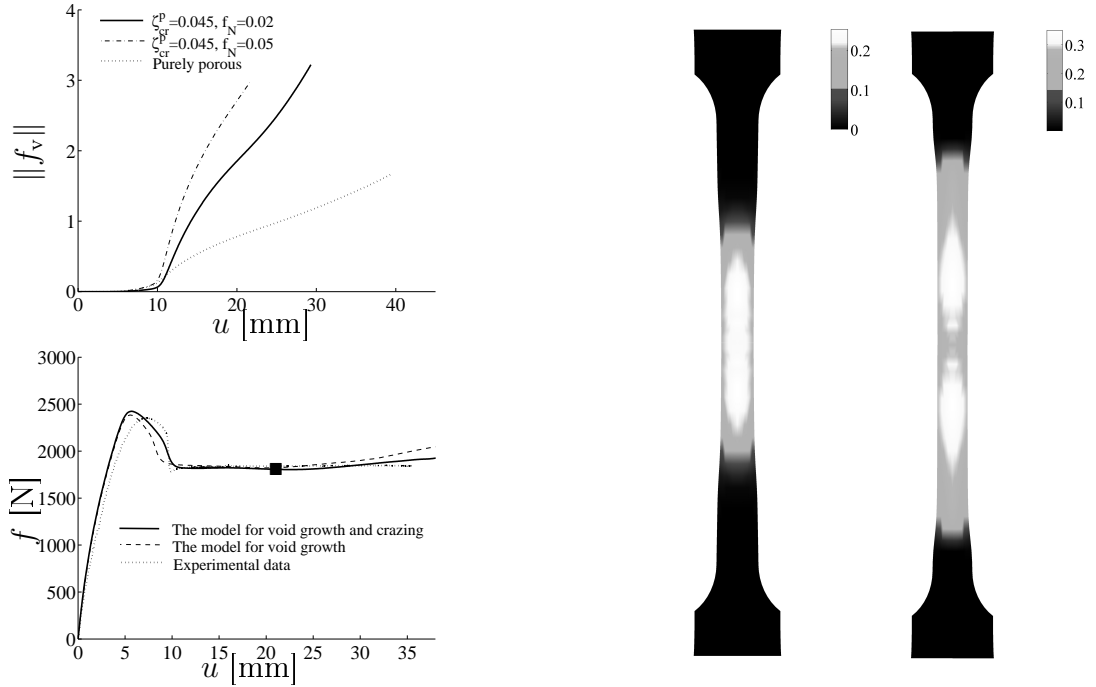
Figure 14: Influence of crazing on void growth, which is represented by the norm of void volume fraction $\|f_v\| := \sqrt{\sum_i (f_{v,i} \cdot f_{v,i})}$ where $f_{v,i}$ are the extrapolated values of void volume fraction at the nodes of the mesh. Influence of void growth and crazing on the overall $f - u$ response. The marker ∎ indicates the position at first craze-initiation. Using $f_N = 0.02$, the deformed shapes at $u = 20$ mm and at $u = 30$ mm are visualized by the void volume fraction f_v. The white color indicates the highest porosity.

The influence of crazing on void growth during localized deformation is shown in Fig. 14. A comparison with the responses of purely porous material reveals that crazing, which initiates once the yield point is passed, increases significantly void growth during the neck. Similar effect was also observed in amorphous entanglement network through MD simulations, cf. [16]. Reducing void nucleation setting $f_N = 0.02$ in (37) compensates for the growth which in turn, as already touched upon, suppresses the initiation of new crazes. The difference can be further illustrated by a comparison of the void volume fractions given in Figs. 9 and 14. Due to crazing, localized

region (in terms of $\bar{\lambda}_{ec}^P$) in the gauge section shows more pronounced intensity of porosity, whereas the area and shape of the porous region remain virtually unaltered during crazing.

To prevent an excessive void growth during crazing, the amount of existing voids as well as their growth need to be limited in the model. Consequences of this restriction are that crazing promotes void nucleation while the dissipation alters primarily due to the stress τ_e in the ligaments between the voids. An excessive void growth during necking is suppressed by choosing the critical strain for craze-initiation to be $\zeta_{cr}^P = 0.42$, which value approximately corresponds to the elongation $u = 21$ mm and to the plastic stretch $\bar{\lambda}_{ec}^P = 1.055$ in the early-stage of hardening. Moreover, crazing is assumed to result from disentanglement in highly concentrated regions of maximum principal stress, which nucleates new micro-voids and allows their coalesce to form initial crazes rather than larger voids. Thus, use is made of an assumption that the growth of existing voids is inhibited by crazing, i.e.

$$\dot{f}_g = \begin{cases} 0 & \text{during crazing,} \\ 3(1 - f_g)D_h^p & \text{otherwise.} \end{cases} \tag{58}$$

Since crazing in a finite element setting evaluates through the integration points, the influence of the mesh does need attention. Simulations with considerably finer mesh, however, indicated only a small mesh-sensitivity on both the $f - u$ response and localization phenomenon. In Fig. 14, both the porous and the crazed response is depicted. It is found that the void volume fraction, albeit it is low in small deformations, has the effect of making the descending portion in the force-elongation curve more gradual. Crazing, however, is seen to compensate this effect. Owing to crazing, premature hardening which appears in the augmented EBPA model predictions for purely porous material is substantially reduced in the model predictions for crazed material. This is in better agreement with the experimental response that shows very stable neck.

Fig. 15 shows the deformed meshes visualized by the plastic stretch $\bar{\lambda}_{ec}^P$, the mean stress

Figure 15: The deformed meshes at a) $u = 20$ mm and b) $u = 33$ mm are visualized by the plastic stretch $\bar{\lambda}_{ec}^P$, mean stress τ_m and by the craze-strain ζ^P. The void fraction parameter in (37) is $f_N = 0.02$ and the rest of the parameters is given in Table 4.

τ_m and the craze-strain ζ^P. The selected stages cover the elongation just prior to crazing and $u = 33$ mm. A glance at the preceding results in Fig. 10 reveals that crazing has no notable influence on the localization of plastic deformation, i.e. the intensity and the rate of expansion remain virtually unaltered. It appears from Fig. 15 that the distribution of $\bar{\lambda}_{ec}^P$ is similar to the ζ^P-distribution which controls craze-initiation. The craze-strain ζ^P in its localized region ranges between $\zeta^P = 0.40 - 0.50$, which values with together the low intensity of the plastic stretching imply that the threshold ζ_t^P for craze-breakdown should be significantly greater than 0.50. In contrast to the expansion of localized deformation, the region of pronounced mean stress rapidly propagates over the gauge section and reaches relatively stable values ranging between $27 - 32$ MPa. Since these values are higher than $0.4 - 0.5$ times the yield stress for PC, craze-initiation, as has previously been pointed out, can be considered as an instantaneous process.
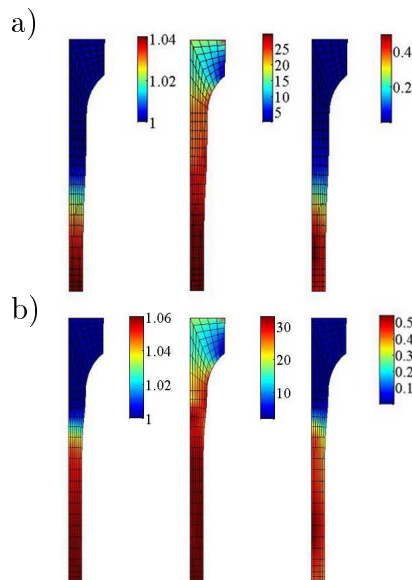
Influence of disentanglement

Based on the idea that entanglements represent topological constraints and on the observation that the topology does not evolve considerably in glassy state, the network density n in state-of-the-art models is taken to be constant during deformation. However, the present numerical results explicitly suggest that a reduction of n should be considered in the models. Since the molecular weight of the polymer remains unchangeable, the total number of statistical links N_A in the material element is constant. In pursuance of the chain density evolves (reduces) with time, N alters (increases) according to the relation $nN = N_A$. By the definition $C_R := nkT$ employed, the reducing strain hardening modulus is attributed to disentanglement. Disentanglement is modeled by assuming that the network density n evolves with time t as

$$\frac{\partial n}{\partial t} = -n\frac{p_0}{\tau_v} \tag{59}$$

where τ_v denotes a time interval, needed that a particular entangled point vanishes, and

$$p_0 = \exp\left(-\frac{U_0 - \beta\Delta b_{\text{eq}}}{kT}\right) \tag{60}$$

is the probability that a particular chain slips through an entangled point. In the above equation, U_0 is the activation energy, β is the activation volume and

$$\Delta b_{\text{eq}} = \sqrt{\text{trace}\left(\frac{1}{2}(\boldsymbol{\beta}^{\text{dev}})^2\right)}$$

represents the difference in network stress between the two strands of a chain connected to a common entangled point, cf. [14] for a more detailed account.
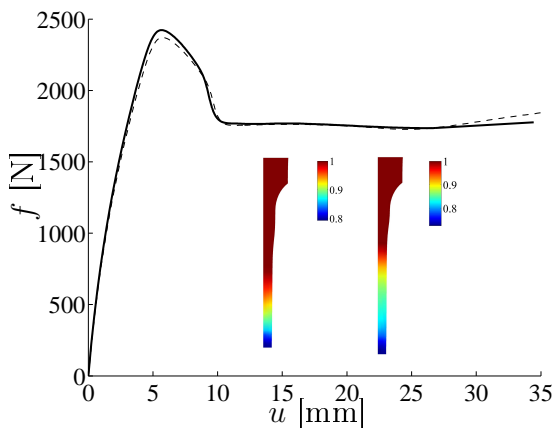

Figure 16: Influence of the reduction of network density n on $f - u$ response (solid line). The dashed line represents the response with a constant network density. The parameters used in (59) are taken from [14]. The deformed shapes at $u = 28$ mm and $u = 36$ mm are highlighted by the network density ratio n/n_0. Using the EBPA model parameters, $n_0 = 3.4 \cdot 10^{27}$ m^{-3}.

When (59) is employed, disentanglement evolves already during softening and numerical simulations indicate a significant increase in void growth during neck. In terms of microstructural characteristics, the free volume between the chains decreases pressure, and consequently the Brownian motion of chains eases and viscosity decreases. Assuming crazing evolves due to disentanglement and a critical amount of porosity for the nucleation of crazes is reached at the end of the softening phase, use is made of an assumption that the growth of existing voids is attenuated during necking, i.e. the transition (58) is employed.

The simulated $f - u$ response in Fig. 16 shows stabilizing effect due to disentanglement, i.e. no obvious tensile limit of stable neck can be observed during elongation up to $u = 35$ mm. Loss of the network density 15% is reached at $u \approx 20$ mm, which value remains almost constant during further elongation. According to the numerical simulations, similar effects cannot be observed if the network density alters without volume changes, i.e. the models for both void growth and crazing need to be applied. It can be concluded that the network density is of a great importance in determining the macroscopic failure through crazing.

5 Conclusions

The capability of state-of-the-art network models to predict inhomogeneous deformation behavior of amorphous glassy polymers was investigated. The two models termed the BPA and the EBPA model, respectively, were implemented in a finite element program and an implicit integration algorithm was derived. Since the polymer network density is considered constant and the volumetric plastic deformation is suppressed in the present models, they are generally inappropriate for modeling damage. The models were calibrated to the force-elongation responses for inhomogeneous deformation acquired from cold drawing experiments on polycarbonate specimens. It was shown that the parameters which were obtained from the calibration to homogeneous deformation cannot be used to satisfactorily predict the experimental response of inhomogeneous deformation. In order to find the mechanisms that are able to explain this discrepancy, the models for void growth, crazing and disentanglement were implemented in a part of the EBPA model.

The simulations showed that the initiation of shear bands promotes and void growth reduces the intrinsic softening in the material, whereas the kinematic hardening is seen to be a driving force for widening of shear bands. It was shown that the EBPA model, in conjunction with the modified Gurson model for void growth, predicts increased porosity and interaction between the voids and less intrinsic softening. As a result, the difference between the calibrated parameters for homogeneous and inhomogeneous deformation considerably decreased.

In order to suppress an excessive void growth during localized deformation and a premature hardening present in the simulations of the cold drawing experiment, the model was augmented also by taking crazing into consideration. In general, however, the strain hardening cannot be solely governed by the stretching of the chain network, but the hardening tends to decrease with the chain density of the polymer network. In the proposed model, crazing is assumed to result from disentanglement in highly concentrated regions of maximum principal stress, which nucleates new micro-voids. However, these voids do not grow, but coalesce to form initial crazes that widen and eventually cause local failure in the material. The numerical results indicated that the plastic stability is essentially controlled by crazing, whereas void growth governs the rate of neck propagation and the amount of intrinsic softening during localized deformation. It was also concluded that the network density plays a pivotal role in determining the type of macroscopic failure through either shear yielding or crazing. The EBPA model augmented by the models for both void growth and crazing was able to predict inhomogeneous deformation behavior well. However, further research is needed to find and model the localization mechanisms also under variable loadings and at different length-scales.

Acknowledgements

References

[1] A. S. Argon. A theory for the low-temperature plastic deformation of glassy polymers. *Philosophical Magazine*, 28(4):839–865, 1973.

[2] O. A. Hasan and M. C. Boyce. A constitutive model for the nonlinear viscoelastic viscoplastic behavior of glassy polymers. *Polym. Engngn. Sci.*, 35:331–344, 1995.

[3] A. C. Steenbrink and E. Van der Giessen. Studies on the growth of voids in amorphous glassy polymers. *Journal of Material Sciences*, 33:3163–3175, 1998.

[4] L. Anand and M. E. Gurtin. A theory of amorphous solids undergoing large deformations, with application to polymeric classes. *Int. J. Solids Structures*, 40:1465–1487, 2003.

[5] L. Anand and B. P. Gearing. On modeling the deformation and fracture response of glassy polymers due shear-yielding and crazing. *Int. J. Solids Structures*, 41:3125–3150, 2004.

[6] A. S. Argon. Craze initiation in glassy polymers - revisited. *Polymer*, 52:2319–2327, 2011.

[7] P. B. Bowden and S. Raha. The formation of micro shear bands in polystyrene and polymethylmethacrylate. *Philosophical magazine*, 22:463–482, 1970.

[8] Y. Tomita and M. Uchida. Characterization of micro- to macroscopic deformation behavior of amorphous polymer with heterogeneous distribution of microstructures. *Int. J. Mech. Sci.*, 45:1703–1716, 2003.

[9] C. G'Sell, J. M. Hiver, and A. Dahoun. Experimental characterization of deformation damage in solid polymers under tension, and its interrelation with necking. *Int. J. Solids Structures*, 39:3857–3872, 2002.

[10] H. G. H. Van Melick. *Deformation and failure of polymer glasses. Doctoral thesis.* University Press Facilities, Eindhoven, 2003.

[11] T. Itoh, K. Yashiro, and Y. Tomita. Molecular dynamic study on deformation of molecular chains in amorphous polymer. In *JSMS Seventh Symposium on Molecular Dynamics*, pages 50–55, 2002.

[12] H. H. Kramer and L. L. Berger. Craze growth and fracture. *Adv. Polym. Sc.*, 91:1–68, 1990.

[13] R. Estevez, M. G. A. Tijssens, and E. Van der Giessen. Modeling of the competition between shear yielding and crazing in glassy polymers. *J. Mech. Phys. Solids*, 48:2585–2617, 2000.

[14] S. Basu, D. K. Mahajan, and E. Van der Giessen. Micromechanics of the growth of a craze fibril in glassy polymers. *Polymer*, 46:7504–7518, 2005.

[15] M. Ishikawa and H. Ogawa. Brittle fracture in glassy polymers. *J. Macromolecules. Sci.-Phys. B 19*, 3:421–443, 1981.

[16] D. K. Mahajan, B. Singh, and S. Basu. Void nucleation and disentanglement in glassy amorphous polymers. *Physical Review E.*, 82:1–8, 2010.

[17] M. Gologanu, J. B. Leblond, G. Perrin, and J. Devaux. *Recent extensions of Gurson model for porous ductile metals. In: Suquet, P. (Ed.), Continuum Micromechanics.* Springer-Verlag, Berlin, 1997.

[18] T. Seeling and E. Van der Giessen. Localized plastic deformation in ternary polymer blends. *Int. J. Solids Structures*, 39:3505–3522, 2002.

[19] K. G. W. Pijnenburg, T. Seeling, and E. Van der Giessen. Successively refined models for crack tip plasticity in polymer blends. *European Journal of Mechanics A/Solids*, 24:740–756, 2005.

[20] F. ZaÃŕri, M. Naït-Abdelaziz, J. M. Gloaguen, and J. M. Lefebvre. Modeling of the elasto-viscoplastic damage behavior of glassy polymers. *Int. J. Plasticity*, 24:945–965, 2008.

[21] F. Zaïri, M. Naït-Abdelaziz, J. M. Gloaguen, and J. M. Lefebvre. A physically-based constitutive model for anisotropic damage in rubber-toughened glassy polymers during finite deformation. *Int. J. Plasticity*, 27:25–51, 2011.

[22] J. R. Rice and D. M. Tracey. On the ductile enlargement of voids in triaxial stress fields. *J. Mech. Phys. Solids*, 17:201–217, 1969.

[23] A. Needleman and V. Tvergaard. An analysis of ductile rupture in notched bars. *J. Mech. Phys. Solids*, 32:461–490, 1984.

[24] H. Y. Subramanya, S. Viswanath, and R. Narasimhan. Constraint effects on multiple void interaction in pressure sensitive plastic solids. *Engng. Fract. Mech.*, 76:1049–1073, 2009.

[25] A. L. Gurson. Continuum theory of ductile rupture by void nucleation and growth: Part I - yield criteria and flow rules for porous ductile media. *ASME J. Engng. Materials Technol.*, 99:2–15, 1977.

[26] V. Tvergaard. Influence of voids on shear bands instabilities under plane strain conditions. *Int. J. Fracture*, 17:389–407, 1981.

[27] E. M. Arruda and M. C. Boyce. Anisotropy and localization of plastic deformation. In J. P. Boehler and A. S. Khan, editors, *Proc. Plasticity*, page 483. Elsevier Applied Science, London, 1991.

[28] E. M. Arruda and M. C. Boyce. Evolution of plastic anisotropy in amorphous polymers during finite straining. *Int. J. Plasticity*, 9:697–720, 1993.

[29] E. M. Arruda, M. C. Boyce, and H. Quintus-Bosz. Effects of initial anisotropy on the finite strain deformation behavior of glassy polymers. *Int. J. Plasticity*, 9:783–811, 1993.

[30] L. Anand and N. M. Ames. On modeling the micro-indentation response of an amorphous polymer. *Int. J. Plasticity*, 22:1123–1170, 2006.

[31] C. Dreistadt, A S. Bonnet, P. Chevrier, and P. Lipinski. Experimental study of the polycarbonate behaviour during complex loadings and comparison with the Boyce, Parks and Argon model predictions. *Materials and Design*, 30:3126–3140, 2009.

[32] S. Holopainen and M. Wallin. Modeling of long-term behavior of amorphous glassy polymers. *ASME J. Engng. Materials Technol.*, 135:1–11, 2012.

[33] E. H. Lee. Elastic-plastic deformation at finite strains. *J. Appl. Mech.*, 36:1–6, 1969.

[34] S. Holopainen. Modeling of the mechanical behavior of amorphous glassy polymers under variable loadings and comparison with state-of-the-art model predictions. *Mechanics of Materials*, 66:35–58, 2013.

[35] K. Hasanpour and S. Ziaei-Rad. Finite element simulation of polymer behavior using a three-dimensional, finite deformation constitutive model. *Comp. Struct.*, 86:1643–1655, 2008.

[36] P. D. Wu and E. Van der Giessen. On improved network models for rubber elasticity and their applications to orientation hardening in glassy polymers. *J. Mech. Phys. Solids*, 41(3): 427–456, 1993.

[37] R. Becker and A. Needleman. Effect of yield surface curvature on necking and failure in porous plastic solids. *J. Appl. Mech.*, 53:491–499, 1986.

[38] Z. L. Zhang, C. Thaulow, and J. Ødegård. A complete Gurson model approach for ductile fracture. *Engng. Fract. Mech.*, 67:155–168, 2000.

[39] C. C. Chu and A. Needleman. A void nucleation effects in biaxially stretched sheets. *ASME J. Engng. Materials Technol.*, 102:249–256, 1980.

[40] M. Wallin. *Modeling of Plasticity at Large Strains. Doctoral Thesis. Report TFHF-1027.* Lund, Sweden, 2003.

[41] M. E. Gurtin. On a framework for small-deformation viscoplasticity: free energy, microforces, strain gradients. *Int. J. Plasticity*, 19:47–90, 2003.

[42] M. E. Gurtin and L. Anand. The decomposition $\boldsymbol{F} = \boldsymbol{F}^e \boldsymbol{F}^p$, material symmetry, and plastic irrotationality for solids that are isotropic-viscoplastic or amorphous. *Int. J. Plasticity*, 21: 1686–1719, 2005.

[43] N. S. Ottosen and M. Ristinmaa. *The Mechanics of Constitutive Modeling.* Elsevier Science, 1 edition, 2005.

[44] B. Coleman and M. E. Gurtin. Thermodynamics with internal state variables. *The Journal of Chemical Physics*, 47:597–613, 1967.

[45] P. Rabier. Some remarks on damage theory. *Int. J. Engng. Sci.*, 27:29–54, 1989.

[46] A. C. Steenbrink, E. Van der Giessen, and P. D. Wu. Void growth in glassy polymers. *J. Mech. Phys. Solids*, 45:405–437, 1997.

[47] H. H. Kramer. Microscopic and molecular fundamentals of crazing. *Advances in Polymer Science*, 52:1–56, 1983.

[48] A. S. Argon and J. G. Hannoosh. Initiation of crazes in polystyrene. *Philosophical Magazine*, 36:1195–1216, 1977.

[49] A. S. Argon. Craze plasticity in low molecular weight diluent-toughened polystyrene. *Journal of Applied Polymer Science*, 72:13–33, 1999.

[50] G. Weber and L. Anand. Finite deformation constitutuve equations and a time integration procedure for isotropic, hyperelastic-viscoplastic solids. *Comput. Methods Appl. Mech. Engng.*, 79:173–202, 1990.

[51] P. Steinmann and E. Stein. On the numerical treatment and analysis of finite deformation ductile single crystal plasticity. *Comput. Methods Appl. Mech. Engng.*, 129:235–254, 1996.

Appendix A. Algorithmic setting of the augmented EBPA model

The EBPA model is implemented in a finite element program for the simulations of inhomogeneous deformation. Since long-term periods are investigated, a fully implicit backward Euler method, which allows large time steps, is applied. To simplify the notation, the subscript n + 1 for the updated state is omitted and the quantities solely at the known state t_n are indicated by the subscript n. The exponential update is applied to the plastic part of the deformation gradient $\boldsymbol{F}^\mathrm{p}$, i.e.

$$\boldsymbol{F}^\mathrm{p} = \exp(\Delta t \bar{\boldsymbol{L}}^\mathrm{p}) \boldsymbol{F}^\mathrm{p}_\mathrm{n}, \tag{A.1}$$

cf. [50]. The tensor exponent in (A.1) is calculated by using the Pade approximation, cf. [51]. Substitution of (A.1) in (1) yields

$$\boldsymbol{F}^\mathrm{e} = \boldsymbol{F} \boldsymbol{F}^{\mathrm{p}-1} = \boldsymbol{F} \boldsymbol{F}^{\mathrm{p}-1}_\mathrm{n} \exp(-\Delta t \bar{\boldsymbol{L}}^\mathrm{p}). \tag{A.2}$$

As with the BPA model, the elastic deformation in the EBPA model is chosen to be irrotational and consequently the elastic rotation $\boldsymbol{R}^\mathrm{e}$ is unity and the plastic spin $\bar{\boldsymbol{W}}^\mathrm{p}$ is nonzero. The plastic spin is numerically solved by introducing an algorithmic plastic spin $\tilde{\boldsymbol{W}}^\mathrm{p}$. Due to the imposed symmetry of $\boldsymbol{F}^\mathrm{e}$, algorithmic plastic spin $\tilde{\boldsymbol{W}}^\mathrm{p}$ is skew-symmetric at the end of the integration interval. Moreover, to specify the orientation of the elastic intermediate configuration, the first component $\boldsymbol{F}^\mathrm{e}_1$ in the decomposition (15) is chosen to be symmetric.

Based on the stress equilibrium (17), the elastic stretching evolves according to

$$\frac{d}{dt}\left(\ln \boldsymbol{v}^\mathrm{e}_2\right) = \frac{1}{\eta}(\boldsymbol{\mathcal{L}}^\mathrm{e}(E) : \ln \boldsymbol{v}^\mathrm{e}_1 - \boldsymbol{\mathcal{L}}^\mathrm{e}(E_1) : \ln \boldsymbol{v}^\mathrm{e}_2). \tag{A.3}$$

The non-linear system of equations are completed by the integration of the internal rate variables and the void volume fraction rates defined by (26), (37) and (58), respectively, i.e.

$$\begin{aligned}
\boldsymbol{R}_1 &:= \boldsymbol{F}^\mathrm{e} - \boldsymbol{F} \boldsymbol{F}^{\mathrm{p}-1}_\mathrm{n} \exp\left(-\Delta t(\bar{\boldsymbol{D}}^\mathrm{p} + \tilde{\boldsymbol{W}}^\mathrm{p})\right), \\
\boldsymbol{R}_2 &:= \boldsymbol{F}^{\mathrm{e},\mathrm{T}} - \boldsymbol{F}^\mathrm{e}, \\
\boldsymbol{R}_3 &:= \tilde{\boldsymbol{W}}^{\mathrm{p},\mathrm{T}} + \tilde{\boldsymbol{W}}^\mathrm{p}, \\
\boldsymbol{R}_4 &:= \boldsymbol{F}^{\mathrm{e},\mathrm{T}}_1 - \boldsymbol{F}^\mathrm{e}_1, \\
\boldsymbol{R}_5 &:= \left((\boldsymbol{\mathcal{I}} + \frac{\Delta t}{\eta}\boldsymbol{\mathcal{L}}^\mathrm{e}(E_1)) : \ln \boldsymbol{v}^\mathrm{e}_2 - \frac{\Delta t}{\eta}\boldsymbol{\mathcal{L}}^\mathrm{e}(E) : \ln \boldsymbol{v}^\mathrm{e}_1 - \ln \boldsymbol{v}^\mathrm{e}_{2,\mathrm{n}}\right)/s_\mathrm{ss}, \\
R_6 &:= (s_1 - s_{1,\mathrm{n}} - \dot{s}_1 \Delta t)/s_\mathrm{ss}, \\
R_7 &:= (s_2 - s_{2,\mathrm{n}} - \dot{s}_2 \Delta t)/s_\mathrm{ss}, \\
R_8 &:= (f_\mathrm{n} - f_{\mathrm{n},\mathrm{n}} - \dot{f}_\mathrm{n} \Delta t), \\
R_9 &:= (f_\mathrm{g} - f_{\mathrm{g},\mathrm{n}} - \dot{f}_\mathrm{g} \Delta t)
\end{aligned} \tag{A.4}$$

where the parameter s_ss was defined in $(26)_1$. During crazing, the rate of plastic deformation $\bar{\boldsymbol{D}}^\mathrm{p}$ is defined by (54), otherwise it evolves according to the flow rule (32). It should be mentioned that the residuals $\boldsymbol{R}_2$ and $\boldsymbol{R}_4$ consist of three and the residuals $\boldsymbol{R}_3$ and $\boldsymbol{R}_5$ of six linearly independent equations. To solve the nonlinear system (A.4) by using the Newton-Raphson method, the state variables are given in the vectorized form, i.e. $\boldsymbol{Y} := [\boldsymbol{F}^\mathrm{e} \ \tilde{\boldsymbol{W}}^\mathrm{p} \ \boldsymbol{F}^\mathrm{e}_1 \ s_1 \ s_2 \ f_\mathrm{n} \ f_\mathrm{g}]$. The solution is given by $\boldsymbol{Y}^{\mathrm{i}+1} = \boldsymbol{Y}^\mathrm{i} + \Delta \boldsymbol{Y}$ where the increment of the internal variables is given by

$$\Delta \boldsymbol{Y} = -\boldsymbol{J}^{-1}\boldsymbol{R}, \text{ and } \boldsymbol{J} := \frac{\partial \boldsymbol{R}}{\partial \boldsymbol{Y}} \tag{A.5}$$

is the Jacobian. The vectorized form $\boldsymbol{R} := [\boldsymbol{R}_1 \ \boldsymbol{R}_2 \ \boldsymbol{R}_3 \ \boldsymbol{R}_4 \ \boldsymbol{R}_5 \ R_6 \ R_7 \ R_8 \ R_9]$ consists of the residuals.

Table 5: Algorithmic update of internal variables based on the multiplicative decomposition of the deformation gradient into an elastic and a plastic part. The elastic part is further decomposed into a purely elastic and a viscous part.

1. Load data: $\boldsymbol{F}$, $\boldsymbol{Y}_n := [\boldsymbol{F}_n^e \; \tilde{\boldsymbol{W}}_n^p \; \boldsymbol{F}_{1,n}^e \; s_{1,n} \; s_{2,n} \; f_{n,n} \; f_{g,n}]$.

2. Set k = 0 and initialize $\boldsymbol{F}^p|_{k=0} = \boldsymbol{F}_n^{e-1}\boldsymbol{F}$, $\boldsymbol{F}_2^e|_{k=0} = \boldsymbol{F}_{1,n}^{e-1}\boldsymbol{F}_n^e$.

3. Implicit update of the internal variables:
   WHILE $\|\boldsymbol{R}\| >$ tol
   (*i*) Compute $\dot{\gamma}^p$ by (24), $\boldsymbol{\beta}$ by (46), $\boldsymbol{\tau}$ by (17) and $\tilde{\boldsymbol{\tau}} := \boldsymbol{\tau} - \boldsymbol{\beta}$.
   (*ii*) Compute $\dot{s}_1$, $\dot{s}_2$ by (26) and $\dot{f}_n$ by (37).
   IF $\tau_m > 0$ and $\tau_1 = \tau^{cr} > 0$ THEN (crazing)
   (*iii*) Update τ^e from (57).
   (*iv*) Compute $\boldsymbol{d}^p$ by (54).
   (*v*) Compute $\dot{f}_g$ by (58).
   ELSE
   (*iii*) Update τ^e from (28).
   (*iv*) Compute $\boldsymbol{d}^p$ by (32).
   (*v*) Compute $\dot{f}_g$ by (36).
   END IF
   (*vi*) Compute the residuals $\boldsymbol{R}$ according to (A.4).
   (*vii*) Compute the Jacobian $J := \partial \boldsymbol{R}/\partial \boldsymbol{Y}$.
   (*viii*) Update internal variables, $\boldsymbol{Y} \leftarrow \boldsymbol{Y}_n + \Delta\boldsymbol{Y}$ by (A.5) and set k $\leftarrow$ k + 1.
   END WHILE LOOP

4. Store updated variables $\boldsymbol{Y} := [\boldsymbol{F}^e \; \tilde{\boldsymbol{W}}^p \; \boldsymbol{F}_1^e \; s_1 \; s_2 \; f_n \; f_g]$ and proceed to the equilibrium iteration for $\boldsymbol{F}$.

The linearization of the stress-strain relation, which is needed in an implicit finite element solution process, is discussed in [32]. The steps of the numerical integration algorithm for updating the internal variables are summarized in Table 5.